An Analytic Model for the Clear-Sky Longwave Feedback

Daniel D.B. Koll[a] , Nadir Jeevanjee[b] , Nicholas J. Lutsko[c]

[a] *Laboratory for Climate and Ocean-Atmosphere Studies, Dept. of Atmospheric and Oceanic Sciences; Peking University; Beijing; China*

[b] *Geophysical Fluid Dynamics Laboratory; Princeton, NJ; USA*

[c] *Scripps Institution of Oceanography; La Jolla, CA; USA*

Corresponding author: Daniel D.B. Koll, dkoll@pku.edu.cn

1

ABSTRACT: Climate models and observations robustly agree that Earth's clear-sky longwave feedback has a value of about -2 W m^{-2} K^{-1}, suggesting that this feedback can be estimated from first principles. In this study, we derive an analytic model for Earth's clear-sky longwave feedback. Our approach uses a novel spectral decomposition that splits the feedback into four components: a surface Planck feedback, and three atmospheric feedbacks from CO_2, H_2O, and the H_2O continuum. We obtain analytic expressions for each of these terms, and the model can also be framed in terms of Simpson's Law and deviations therefrom. We validate the model by comparing it against line-by-line radiative transfer calculations across a wide range of climates. Additionally, the model qualitatively matches the spatial feedback maps of a comprehensive climate model. For present-day Earth, our analysis shows that the clear-sky longwave feedback is dominated by the surface in the global mean and in the dry subtropics; meanwhile, atmospheric feedbacks from CO_2 and H_2O become important in the inner tropics. Together, these results show that a spectral view of Earth's clear-sky longwave feedback elucidates not only its global-mean magnitude, but also its spatial pattern and its state-dependence across past and future climates.

SIGNIFICANCE STATEMENT: The climate feedback determines how much our planet warms due to changes in radiative forcing. For more than 50 years scientists have been predicting this feedback using complex numerical models. Except for cloud effects the numerical models largely agree, lending confidence to global warming predictions, but nobody has yet derived the feedback from simpler considerations. We show that Earth's clearsky longwave feedback can be estimated using only pen and paper. Our results confirm that numerical climate models get the right number for the right reasons, and allow us to explain regional and state variations of Earth's climate feedback. These variations are difficult to understand solely from numerical models but are crucial for past and future climates.

1. Introduction

Earth's climate sensitivity is a crucial factor in understanding and predicting climate change. While uncertainty in climate sensitivity is dominated by cloud feedbacks, the magnitude of climate sensitivity is largely set by the clear-sky longwave feedback, λ_{LW}. Early studies estimated λ_{LW} to be -2.2-2.3 W m^{-2} K^{-1} (Manabe and Wetherald 1967; Budyko 1969). These estimates were impressively close to the current best estimates from climate models and observations, which agree on a fairly narrow range for λ_{LW} of about -1.8 to -2.2 W m^{-2} K^{-1} (Andrews et al. 2012; Chung et al. 2010; Kluft et al. 2019; Zhang et al. 2020; Zelinka et al. 2020). By contrast, the recent Sherwood et al. (2020) assessment estimated the total cloud feedback to be both smaller in magnitude and less certain at +0.45 ± 0.33 W m^{-2} K^{-1}.

The robustness of the clear-sky longwave feedback suggests that one should be able to understand and describe its governing physics in fairly simple form. A simple model for λ_{LW} would provide definitive support for the value of -2 W m^{-2} K^{-1} derived from observations and climate models. It would also allow us to understand the state-dependence of λ_{LW}: at warm enough temperatures Earth's atmosphere transitions to a runaway state, in which λ_{LW} becomes zero or even changes sign, but it is unclear how λ_{LW} varies between today's value and the runaway limit. Similarly, there is a long-standing interest in using paleoclimate proxies to constrain present-day climate sensitivity (Tierney et al. 2020), but this effort suffers from uncertainty regarding the state-dependence of climate feedbacks (Meraner et al. 2013; Bloch-Johnson et al. 2015). Finally, geographic variation in feedbacks and their importance for the so-called pattern effect is an ongoing topic of research

(Armour et al. 2013; Andrews et al. 2015, 2018) , but if λ_{LW} has state-dependence then that dependence should also influence the spatial pattern of λ_{LW}. For example, if the global-mean λ_{LW} was different in past climates due to changes in the global-mean surface temperature, then present-day λ_{LW} should show regional variation due to Earth's surface temperature pattern, suggesting a close link between state-dependence and spatial-dependence of λ_{LW}.

One of the earliest models for λ_{LW} was proposed by Simpson (1928a), who found that an atmosphere that is optically thick due to water vapor would have a clear-sky longwave feedback that is approximately zero, suggesting Earth should be in a runaway greenhouse. Although this early model was abandoned by Simpson (1928b) as being overly simplistic, Ingram (2010) resolved the Simpsonian "paradox" by separating out the parts of Earth's outgoing radiation spectrum that are optically thick due to water vapor (and for which λ_{LW} is approximately zero) from the optically thin "window" region. Koll and Cronin (2018) subsequently quantified Ingram's argument: using fixed relative humidity (RH), single-column calculations they argued that for present-day Earth the clear-sky longwave feedback is dominated by the surface:

$$\lambda_{LW} \quad \approx \quad \lambda_{\mathrm{surf}}. \tag{1}$$

Here λ_{surf} is the surface Planck feedback, which is smaller than a blackbody's feedback because greenhouse gases block the surface's emission outside the spectral window. Meanwhile, the atmosphere itself contributes less to λ_{LW} in the present climate, and so to first order its contribution can be ignored. It follows that atmospheric feedback terms which are often the focus of climate model or observational analyses – the atmospheric component of the Planck feedback, the lapse-rate feedback and the water vapor feedback – roughly cancel (Koll and Cronin 2018; Jeevanjee et al. 2021a).

The match between λ_{LW} and the surface Planck feedback λ_{surf} in Equation 1 is not exact, however. Follow-up work found that λ_{surf} only accounts for 50-90% of λ_{LW} in different regions, with about 60% in the global mean (Raghuraman et al. 2019; Feng et al. 2022), implying a gap in the argument of Koll and Cronin (2018). Similarly, Seeley and Jeevanjee (2021) showed that in hot, high-CO_2 climates λ_{surf} becomes negligible yet λ_{LW} does not go to zero. As the surface warms the atmosphere is still able to increase its emission to space in spectral regions that are dominated by CO_2. This emission mostly comes from the upper atmosphere, and gives rise to a

spectral CO_2 "radiator fin" feedback. The existence of a CO_2 feedback means λ_{LW} must depend on CO_2 concentration, and thus must have CO_2 state-dependence. Moreover, the CO_2 feedback has to depend on the atmospheric lapse rate: if the atmosphere was isothermal with zero lapse rate, CO_2's forcing and feedback would both have to be zero, in line with previous work which tried to quantify the dependence of CO_2 forcing on the lapse rate (Huang and Bani Shahabadi 2014; Dufresne et al. 2020), even if the details of the forcing mechanism are still disputed (Seeley 2018; Romps et al. 2022). So while the "surface-only" feedback picture from Koll and Cronin (2018) gives a reasonable first-order approximation to λ_{LW}, more terms are needed to describe λ_{LW} quantitatively.

In this study, we aim to derive a simple model of Earth's feedback that can quantitatively capture the magnitude of λ_{LW} as well as its state-dependence and regional variations. The model decomposes λ_{LW} into the surface Planck feedback (λ_{surf}) plus three atmospheric terms: a CO_2 band feedback (λ_{co_2}), a non-Simpsonian water vapor band feedback ($\lambda_{\text{H}_2\text{O}}$), and a destabilizing water vapor continuum feedback (λ_{cnt}). Although these feedbacks are less familiar, they represent the different substances through which Earth gives longwave radiation off to space, and how each substance changes its emission under surface warming. As shown below, expressions can be derived for each spectral feedback term starting from the basic equations of radiative transfer. These expressions can be interpreted as a global-mean model for λ_{LW} or in terms of local feedbacks (Feldl and Roe 2013; Armour et al. 2013; Bloch-Johnson et al. 2020). That is, each atmospheric column is treated as an isolated 1D system whose longwave feedback depends on its local surface temperature. We validate the model (and the utility of the spectral decomposition) by comparing it against calculations with a line-by-line radiation code.

Our model of λ_{LW} is based on spectroscopic thinking and hence represents a different perspective than the conventional decomposition which breaks the clear-sky longwave feedback into Planck, Lapse-rate and Water Vapor feedbacks (e.g., Soden et al. 2008; Sherwood et al. 2020; Zelinka et al. 2020). The conventional decomposition has been an important tool for understanding λ_{LW} and for diagnosing the physics governing outgoing longwave radiation in climate models. However, it also obscures large cancellations between the atmospheric part of the Planck feedback, the Lapse-rate feedback and the Water Vapor feedback (Held and Shell 2012; Koll and Cronin 2018; Jeevanjee et al. 2021a). By obscuring these cancellations the conventional decomposition can give a false

impression of the uncertainty of climate models. The same cancellations also make it difficult to understand the state-dependence of λ_{LW} – Planck, Lapse-rate and Water Vapor feedbacks all increase in a warmer climate, but it is far from obvious how these changes add up to affect λ_{LW} (Meraner et al. 2013). Building on previous discussions of spectral feedbacks (e.g., Huang et al. 2010, 2014; Koll and Cronin 2018; Pan and Huang 2018; Seeley and Jeevanjee 2021; Jeevanjee et al. 2021a; Kluft et al. 2021; Feng et al. 2022), our goal in this paper is to show that the issues that arise in the conventional decomposition can be resolved by viewing λ_{LW} in terms of its spectral components instead.

The layout of the rest of this paper is as follows. Section 2 discusses several preliminaries which are necessary for the main derivations: an idealized Clausius-Clapeyron relation, an analytic approximation for moist lapse rates and idealized band models for H_2O and CO_2 spectroscopy. Section 3 lays out our spectral framework and introduces the emission-level approximation, our spectral decomposition of λ_{LW} and a description of the numerical line-by-line calculations. Section 4 derives analytic expressions for Earth's emission temperature in different parts of the spectrum, which are then used in Section 5 to derive analytic feedbacks. Our expressions compare favorably against the state-dependence of λ_{LW} from line-by-line calculations. Next, Section 6 uses these results to understand the spatial pattern of Earth's clear-sky longwave feedback. We generate global maps of Earth's clear-sky longwave feedback using a radiative kernel and climate model data. We then show that our analytic expressions recover qualitatively similar feedback patterns, which implies that the spatial pattern of λ_{LW} can be largely understood using our analytic model. Breaking λ_{LW} up into surface versus atmospheric terms, we find that the surface dominates λ_{LW} in the global-mean as well as in the dry subtropics, with a spatial pattern set by the pattern of atmospheric relative humidity, while atmospheric feedbacks become significant in the inner tropics, with spatial patterns that are set by regional lapse rate changes under warming. The manuscript closes in Section 7 with a conclusion and broader discussion of the results.

2. Preliminaries

Our goal is to derive the longwave feedback of a cloud-free vertical column of atmosphere. The column's state can be specified using five parameters: T_s, γ_{lr}, RH, q_{co_2} and T_{strat}. Here T_s is the surface temperature, $\gamma_{lr} \equiv d\ln T/d\ln p$ is the temperature lapse rate, RH is the relative humidity,

138 q_{co_2} is the CO$_2$ mass mixing ratio and T_{strat} is the stratospheric temperature. We idealize the state

139 of the column by treating γ_{lr}, RH, and q_{co_2} as vertically uniform; all are defined more precisely

140 below. Similarly, we approximate the stratosphere as isothermal.

a. Clausius-Clapeyron

Saturation vapor pressure over liquid water $e^*(T)$

Reference (Huang 2018)
$e^* = e_0^* \exp[-\frac{R_v}{L_v}(\frac{1}{T} - \frac{1}{T_0})]$
$e^* = e_0^* (\frac{T}{T_0})^{\gamma_{wv}}$
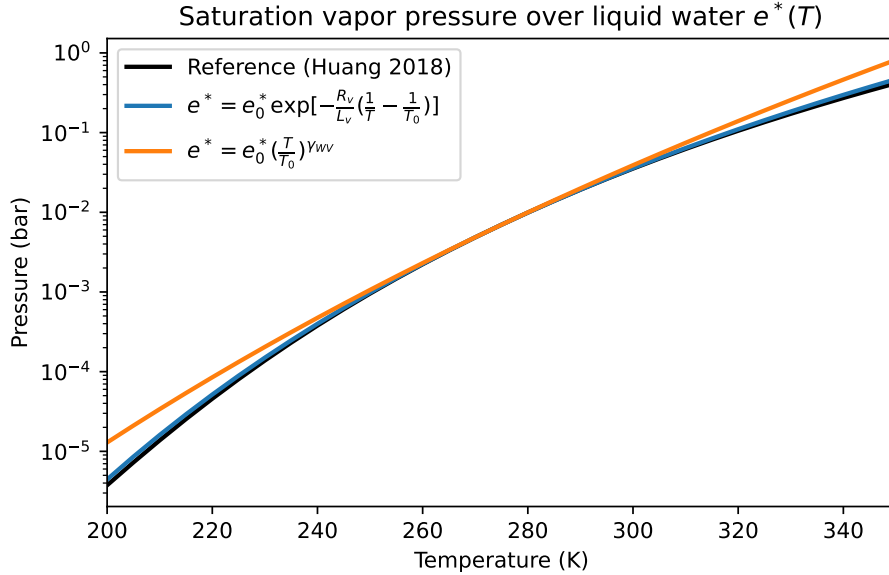
142 FIG. 1. Different approximations to the Clausius-Clapeyron relation. Black: fit based on experimental

143 data (Huang 2018). Blue: the commonly-used quasi-exponential approximation. Orange: the power law

144 approximation used in this work. The saturation vapor pressure is with respect to liquid water. In this plot

145 (T_0, e_0^*) are set equal to the triple point values of H$_2$O, so $\gamma_{wv} = 19.8$.

146 The Clausius-Clapeyron relation governs the temperature-dependence of the saturation vapor

147 pressure $e^*(T)$ and is an essential element of our analytic model. The Clausius-Clapeyron re-

148 lation is often solved by ignoring the temperature-dependence of the latent heat of vaporization,

149 $d \ln e^*/d \ln T = L_v(T)/(R_v T) \approx L_v(T_0)/(R_v T)$, which leads to the quasi-exponential approximation

$$e^* \approx e_0^*(T_0) \exp\left[-\frac{L_v(T_0)}{R_v} \left(\frac{1}{T} - \frac{1}{T_0} \right) \right]. \tag{2}$$

150 This quasi-exponential form does not lead to closed-form analytic expressions in the equations

151 of radiative transfer, however, so we require a simpler form of the Clausius-Clapeyron rela-

7

tion. We obtain this by approximating the Clausius-Clapeyron relation further as $d\ln e^*/d\ln T = L_v(T)/(R_v T) \approx$ const, which leads to a simple power law between temperature and saturation vapor pressure (Koll and Cronin 2019),

$$e^* \approx e_0^*(T_0)\left(\frac{T}{T_0}\right)^{\gamma_{\mathrm{wv}}},\tag{3}$$

where

$$\gamma_{\mathrm{wv}} \equiv \frac{L_v(T_0)}{R_v T_0}.\tag{4}$$

Here T_0 is an arbitrary reference temperature around which we are approximating the saturation vapor pressure as a power law. We emphasize that T_0 is effectively a thermodynamic constant and does not change with surface warming. The non-dimensional power law exponent is large and reflects the steep rise of e^* with temperature; at Earth-like temperatures, $\gamma_{\mathrm{wv}} \approx 20$. The fractional increase in saturation vapor pressure per unit warming is $d\ln e^*/dT = \gamma_{\mathrm{wv}}/T \sim 7\%/\mathrm{K}$, in line with other Clausius-Clapeyron approximations.

Figure 1 compares the approximations in Equations 2 and 3 against a fit based on experimental data (Huang 2018). Considering that a typical tropical atmospheric column spans the vertical temperature range $200-300$ K, the quasi-exponential approximation is very accurate, whereas our power law approximation only matches to roughly a factor of two. Nevertheless, as shown below, this accuracy is good enough to match numerical calculations.

b. Bulk moist lapse rate

The vertical temperature-pressure profile of an atmospheric column can be specified via the lapse-rate exponent

$$\gamma_{\mathrm{lr}} = d\ln T/d\ln p,\tag{5}$$

where p is pressure. For a dry adiabat the lapse rate exponent is vertically uniform, $\gamma_{\mathrm{lr}} = R_d/c_p \approx 2/7$. For a moist atmosphere γ_{lr} varies both as a function of temperature and pressure, but due to the latent heat release in a convecting parcel it is generally smaller than the dry lapse rate: $\gamma_{\mathrm{lr}} \leq R_d/c_p$.

In order to obtain analytically tractable expressions we would like to treat γ_{lr} as constant in the vertical even for a moist column, so we diagnose a bulk γ_{lr} using the surface and tropopause values
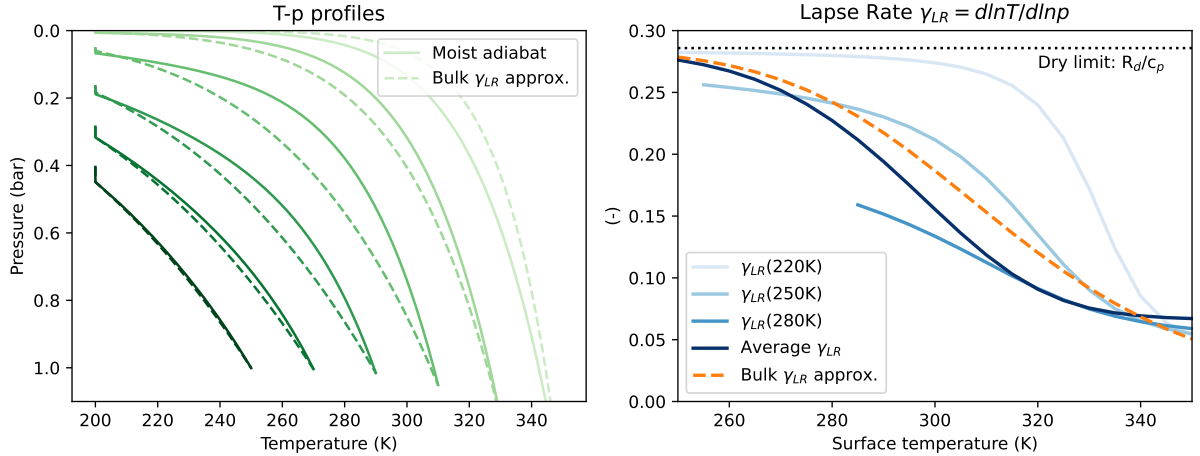
FIG. 2. Moist adiabatic lapse rates versus our analytic approximation. Left: Pressure-Temperature profiles following a moist adiabat (solid) and following the bulk lapse rate approximation (dashed). Right: adiabatic lapse rate γ_{lr} numerically computed at three fixed temperature levels inside the troposphere (light blue), compared with the bulk approximation in Equation (9) (orange). Note that $\gamma_{lr}(T)$ is undefined if T is larger than the surface temperature T_s. The average γ_{lr} (dark blue) is a mass-weighted mean of all numerical lapse rates inside the troposphere, $1/(p_s - p_{tp}) \times \int_{p_{tp}}^{p_s} \gamma_{lr} dp$.

of (T, p):

$$\gamma_{lr} \approx \frac{\ln(T_{tp}/T_s)}{\ln(p_{tp}/p_s)}. \tag{6}$$

Assuming that the tropopause temperature stays constant in response to surface temperature changes, in accord with the FAT/FiTT hypothesis (Hartmann and Larson 2002; Seeley et al. 2019), then all that is needed is an expression for how p_{tp} depends on T_s. We can derive such an expression by first obtaining an expression for the tropopause height z_{tp}, following Romps (2016). From MSE conservation along an undilute moist adiabat between the surface and tropopause,

$$z_{tp} \approx \frac{1}{g} \left(c_p(T_s - T_{tp}) + L_v q_s^* \right), \tag{7}$$

where q_s^* is the mass mixing ratio of water at saturation, q^*, evaluated at the surface and we neglect q^* at the tropopause. p_{tp} can then be obtained as

$$p_{tp} = p_s e^{-z_{tp}/H}, \tag{8}$$

9

where H is the scale height of pressure ($= \frac{R_d T_{av}}{g}$) and $T_{av} \equiv (T_s + T_{tp})/2$. Plugging this into (6) yields

$$\gamma_{lr} \approx \frac{R_d T_{av} \ln(T_s/T_{tp})}{c_p(T_s - T_{tp}) + L_v q_s^*}. \tag{9}$$

One can show that Equation 9 correctly reduces to the dry lapse rate $\gamma_{lr} = R_d/c_p$ by setting $q_s^* = 0$ and series expanding the logarithm, assuming $T_s - T_{tp} \ll T_{tp}$. In practice the latter assumption is not strictly true but the resulting deviation from the dry adiabat is small even for a 100 K difference between surface and tropopause.

According to the bulk approximation, γ_{lr} is constant in the vertical and varies only in response to climatic changes (e.g., changes in surface temperature). One can then integrate Equation 5 to solve for the column's temperature-pressure profile. This leads to a power law similar to a dry adiabat,

$$T(p) = T_s \left(\frac{p}{p_s}\right)^{\gamma_{lr}(T_s)}, \tag{10}$$

where the only difference to a dry adiabat is that now the lapse rate depends on surface temperature.

Figure 2 (left) compares profiles based on Equation 10 to moist adiabatic profiles. The moist adiabats are obtained by numerically integrating a generalized form of the moist adiabat which does not approximate water vapor as a dilute substance and thus remains valid at high temperatures (Ding and Pierrehumbert 2016). In all cases, the tropopause temperature is assumed to be fixed and equal to $T_{strat} = 200$ K. The analytic profiles given by Equation 10 produce a reasonable fit to the moist adiabats, though at surface temperatures below 340 K they produce slightly colder tropospheres. The tropopause pressure is accurately reproduced, as the analytic profiles always reach the tropopause at roughly the same point as the moist adiabats.

Figure 2 (right) compares the T_s-dependence of γ_{lr}. First, the moist adiabatic $T(p)$ profiles shown in Figure 2 (left) are used to numerically compute γ_{LR} at individual levels of the troposphere. Because our bulk expression for γ_{LR} only depends on temperature, and not pressure, the moist adiabatic values of γ_{LR} are similarly shown at fixed temperature levels. Additionally, for each adiabatic $T(p)$ profile we compute the average moist lapse rate using a mass-weighted mean, $1/(p_s - p_{tp}) \times \int_{p_{tp}}^{p_s} \gamma_{lr} dp$. Figure 2 shows that our analytic approximation captures the T_s-dependence of the average moist lapse rate relatively well, though this general agreement can obscure significant differences at individual levels. For example, our analytic approximation of

10

γ_{lr} deviates by more than a factor of two from the moist-adiabatic γ_{lr} at the $T = 220$ K level. We will show below that these details of atmospheric lapse rates do not have a major impact on Earth's longwave feedback at low surface temperatures, but they become increasingly important above ~ 300 K.

c. H_2O and CO_2 spectroscopy

The third ingredient for our derivations is a model of H_2O and CO_2 spectroscopy. We follow previous studies and model the absorption cross-sections of H_2O and CO_2 as log-linear band shapes. Despite the simplicity of these models, they are able to explain numerous features of Earth's climate, including the logarithmic nature of CO_2 forcing, the temperature-dependence of Earth's surface feedback and the vertical structure of radiative cooling (Crisp et al. 1986; Pierrehumbert 2010; Wilson and Gea-Banacloche 2012; Koll and Cronin 2018; Jeevanjee and Fueglistaler 2020; Romps et al. 2022). Because we explore feedbacks over a wide range of temperatures, we additionally need to account for the H_2O continuum. We do so by approximating the continuum as a grey absorber.

For CO_2, the absorption cross-section is

$$\kappa_{\mathrm{co}_2} = \kappa_0 \left(\frac{p}{p_0} \right) \exp \left(-\frac{|\nu - \nu_0|}{l_\nu} \right), \tag{11}$$

where κ_0 is the absorption cross-section in the center of the band, p_0 is a reference pressure, ν is wavenumber, ν_0 the wavenumber of the center of the band and l_ν the decay rate of the absorption cross-section in wavenumber space. Previous work fit these parameters to the CO_2 absorption spectrum at a reference pressure of $p_0 = 0.1$ bar (Jeevanjee et al. 2021b). Because the choice of reference pressure is arbitrary, we here rescale the fits to the dry surface pressure in our calculations (i.e., the surface pressure excluding the contribution of water vapor), $p_0 = 1$ bar. The resulting values are $\kappa_0 = 500$ m^2/kg, $\nu_0 = 667.5$ cm^{-1} and $l_\nu = 10.2$ cm^{-1}.

H_2O band absorption can similarly be modeled using a log-linear shape, though one has to account for the fact that H_2O has two bands which are relevant for Earth's longwave feedback. The rotation band determines H_2O absorption at wavenumbers less than 1000 cm^{-1} and the vibration-rotation

11
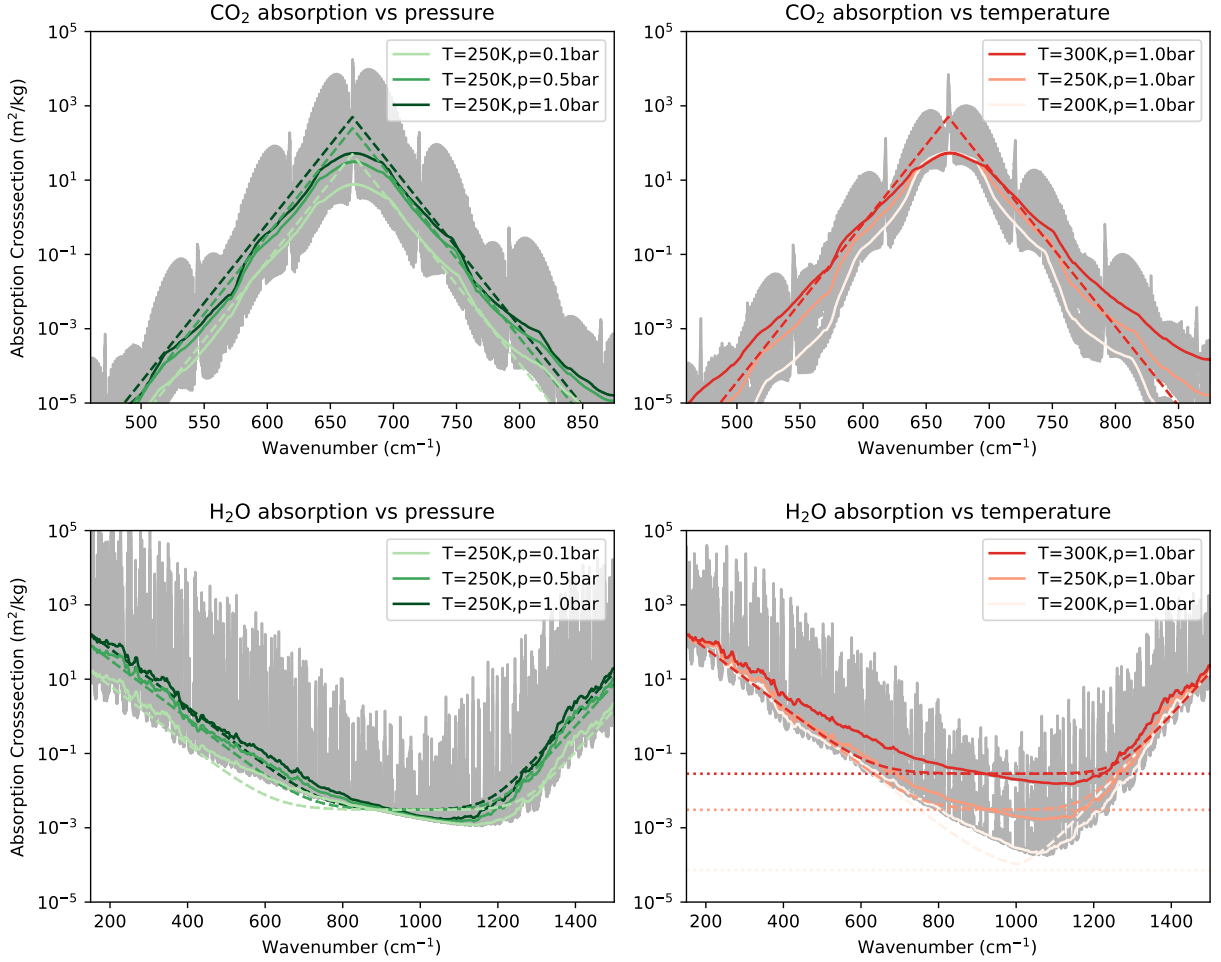
FIG. 3. Idealized band models compared against the absorption cross-sections of CO_2 (top row) and H_2O (bottom). Grey envelopes show cross-sections computed at line-by-line spectral resolution, solid lines are the cross-sections smoothed by a median filter with width 25 cm^{-1}. Dashed lines are the band models for CO_2 and H_2O bands (the sum of line and continuum absorption), while dotted lines show the grey H_2O continuum model only. The CO_2 band model assumes the absorption cross-section is independent of temperature, so only one dashed line is shown in the top right.

band at wavenumbers larger than 1000 cm^{-1}. We model these two bands as

$$
\kappa_{\mathrm{H_2O},line} \quad = \quad \left(\frac{p}{p_0}\right) \max\left[\kappa_{\mathrm{rot}}\exp\left(-\frac{|\nu - \nu_{\mathrm{rot}}|}{l_{\mathrm{rot}}}\right), \kappa_{\mathrm{v-r}}\exp\left(-\frac{|\nu - \nu_{\mathrm{v-r}}|}{l_{\mathrm{v-r}}}\right)\right]. \tag{12}
$$

12

The first term in the max(...) expression represents the rotation band, which dominates at low wavenumbers, while the second term represents the vibration-rotation band at high wavenumbers. The factor p/p_0 in front of both H_2O and CO_2 cross-sections reflects pressure broadening: under present-Earth conditions CO_2 and H_2O absorption lines become wider due to collisions of those molecules with the background air (N_2 or O_2). This has the overall effect that both gases become more efficient absorbers at higher pressure.

In contrast to the CO_2 and H_2O bands, the H_2O continuum is dominated by self broadening so the continuum cross-section is independent of pressure and instead scales as $\propto e = \mathrm{RH}e^*$. Although continuum absorption is not uniform with respect to wavenumber, its spectral dependence is significantly weaker than the H_2O or CO_2 bands. We therefore approximate the continuum as a grey absorber and write

$$\kappa_{\mathrm{H_2O},cnt} = \kappa_{\mathrm{cnt}} \, \mathrm{RH} \, \frac{e^*(T)}{e_0^*} \left(\frac{T}{T_0}\right)^{-a}, \tag{13}$$

where the dimensionless exponent a captures the direct temperature-dependence which acts to weaken the continuum (Pierrehumbert 2010). The total H_2O cross-section is the sum of line and continuum absorption, $\kappa_{\mathrm{H_2O}} = \kappa_{\mathrm{H_2O},line} + \kappa_{\mathrm{H_2O},cnt}$. Because the line opacity decreases exponentially away from H_2O band centers, the total opacity becomes largely dominated by the continuum in the window region around ~ 1000 cm^{-1}.

Our model of H_2O spectroscopy has eight parameters: κ_{rot}, l_{rot}, ν_{rot}, $\kappa_{\mathrm{v-r}}$, $l_{\mathrm{v-r}}$, $\nu_{\mathrm{v-r}}$, κ_{cnt}, a. We set $\nu_{\mathrm{rot}} = 150$ cm^{-1} and $\nu_{\mathrm{v-r}} = 1500$ cm^{-1}, and fit the remaining parameters using the median-smoothed H_2O cross-sections shown in Figure 3 across the wavenumber range 150 cm^{-1} $\leq \nu \leq 1500$ cm^{-1}. The results are sensitive to the smoothing procedure, that is whether one uses a geometric mean or a median. Because the average transmission across a spectral band tends to be dominated by the most optically thin frequencies (Pierrehumbert 2010), we use a median filter. To perform the fits we use the non-linear least-squares algorithm `scipy.optimize.curve_fit`, with a reference temperature of T_0=300 K. We first fit the parameters κ_{rot}, l_{rot}, $\kappa_{\mathrm{v-r}}$, $l_{\mathrm{v-r}}$ to H_2O line opacities only, and then use these parameters to fit κ_{cnt} and a to H_2O cross-sections that include both line and continuum opacity. The resulting values are $\kappa_{\mathrm{rot}} = 165$ m^2/kg, $l_{\mathrm{rot}} = 55$ cm^{-1}, $\kappa_{\mathrm{v-r}} = 15$ m^2/kg, $l_{\mathrm{v-r}} = 38$ cm^{-1}, $\kappa_{\mathrm{cnt}} = 3 \times 10^{-3}$ m^2/kg and $a = 7$, which broadly match the H_2O fits

previously reported in Jeevanjee and Fueglistaler (2020). Table 1 summarizes the thermodynamic and spectral parameters used in this paper.

Figure 3 compares the idealized band models with line-by-line absorption cross-sections. Overall, the shape of the cross-sections is captured fairly well. The median CO_2 and H_2O cross-sections scale linearly with total pressure, as expected for pressure-broadening. The increasing H_2O absorption in response to warming around 1000 cm^{-1} is also qualitatively captured by our grey continuum model, even though the H_2O continuum itself is actually not grey.

Figure 3 (right plots) shows that the slopes of the CO_2 and H_2O bands flatten as temperature increases, with roughly constant opacity in the band centers but increasing opacity in the band wings. This behavior is not captured by our simple models. Physically, absorption band slopes can depend on temperature due to the shifting population of different molecular excitation states. For example, the wings of the 667 cm^{-1} CO_2 band consist of multiple smaller bands that correspond to transitions between excited states of CO_2 (so-called hot bands), while the center of the CO_2 band is dominated by transitions to/from the ground state of CO_2. As temperature rises more CO_2 molecules leave the ground state and access excited states, which in turn preferentially increases the opacity in the wings of the CO_2 band. To keep our parameterizations simple, however, we do not attempt to model the temperature-dependence of the band slopes.

3. Spectral Framework

a. The emission-level approximation

To decompose the net longwave feedback into its spectral components we first need to consider the outgoing longwave flux (OLR) of a vertical column. At a spectral wavenumber ν, the column's longwave flux varies vertically according to the monochromatic optical thickness τ^* and the angle $\cos(\theta)$ with which radiation propagates through the column. Assuming that the atmosphere's longwave radiation follows a known angular distribution, e.g., isotropic, these quantities can be combined into the vertical coordinate $\tau = \tau^*/\cos(\bar{\theta})$. Here $\cos(\bar{\theta})$ describes the average angle of propagation, and τ varies from $\tau = 0$ at the TOA to $\tau = \tau_{\text{surf}}$ at the surface (e.g. Pierrehumbert 2010). The column's OLR is then equal to

$$\text{OLR} = \int_0^\infty \pi B_\nu(T_s) e^{-\tau_{\text{surf}}} \, d\nu + \int_0^\infty \int_0^{\tau_{\text{surf}}} \pi B_\nu(T(\tau)) e^{-\tau} \, d\tau \, d\nu. \quad (14)$$

TABLE 1. List of parameters and, where applicable, assumed values.

Parameter name	Explanation	Assumed value
Thermodynamic parameters		
T_0	Reference temperature for saturation vapor pressure power-law	300 K
γ_{wv}	Exponent in saturation vapor pressure power-law	18
γ_{lr}	Exponent in bulk lapse rate temperature-pressure power-law	Computed using Eqn. 9 (Section 5), or derived from data (Section 6)
Spectral parameters		
$\cos(\bar{\theta})$	Inverse angular diffusivity factor	3/5
p_0	Reference pressure for absorption cross-sections	1 bar
κ_0	Absorption cross-section in center of CO_2 band	500 m^2/kg
ν_0	Wavenumber of the center of the CO_2 band	667.5 cm^{-1}
l_ν	Decay rate of the CO_2 absorption cross-section in wavenumber space	10.2 cm^{-1}
κ_{rot}	Absorption cross-section in center of H_2O rotation band	165 m^2/kg
ν_{rot}	Wavenumber of the center of the H_2O rotation band	150 cm^{-1}
l_{rot}	Decay rate of the H_2O absorption cross-section in wavenumber space in the rotation band	55 cm^{-1}
κ_{v-r}	Absorption cross-section in center of H_2O vibration-rotation band	15 m^2/kg
ν_{v-r}	Wavenumber of the center of the H_2O vibration-rotation band	1500 cm^{-1}
l_{v-r}	Decay rate of the H_2O absorption cross-section in wavenumber space in the vibration-rotation band	38 cm^{-1}
κ_{rot}	Grey absorption cross-section of H_2O continuum	3×10^{-3} m^2/kg
a	Exponent of H_2O continuum temperature-dependence	7
Analytic model parameters		
T_{strat}	Stratospheric temperature	200 K
c_{surf}	Scaling constant for surface feedback	0.8 (bulk lapse rate)/0.8 (moist adiabat)
c_{H_2O}	Scaling constant for H_2O band feedback	0.6 (bulk lapse rate)/1.0 (moist adiabat)
c_{cnt}	Scaling constant for H_2O continuum feedback	0.4 (bulk lapse rate)/0.4 (moist adiabat)
c_{co_2}	Scaling constant for CO_2 band feedback	0.7 (bulk lapse rate)/0.9 (moist adiabat)

The optical thicknesses τ and τ_{surf} are functions of ν, so the order of integration cannot be switched. Physically, the first term corresponds to the surface's emission to space, while the second term corresponds to an integral of the emission coming from each vertical level in the atmosphere.

The emission-level or radiating-level approximation states that the atmosphere's emission to space (the second integral in Equation 14) originates from the vertical level at which optical thickness τ is order unity. The intuition behind the emission-level approximation is that levels of the atmosphere for which $\tau \ll 1$ are optically thin and do not contribute much to the TOA flux, while most emission from levels with $\tau \gg 1$ is absorbed by the overlying atmosphere and so its contribution to the TOA flux is also small. The emission level has been defined at slightly different values of τ, but all definitions agree on a value of order unity (Pierrehumbert 2010; Jeevanjee et al. 2021b). For simplicity, we define the emission level here as the level at which $\tau = 1$. The temperature at this level is then the emission level temperature, $T_{rad} \equiv T(\tau = 1)$, so

$$\text{OLR} \approx \int_0^\infty \pi B_\nu(T_s) e^{-\tau_{surf}} \, d\nu + \int_0^\infty \pi B_\nu(T_{rad}(\nu)) \, d\nu. \tag{15}$$

313 Given the emission-level approximation, the clear-sky longwave feedback is determined by how
314 the surface emission and the atmospheric emission change in response to warming,

$$
\begin{aligned}
-\lambda_{LW} &= \frac{d\text{OLR}}{dT_s} \\
&\approx \int_0^\infty \pi \frac{dB_\nu}{dT}|_{T_s} e^{-\tau_{\text{surf}}} d\nu + \int_0^\infty \pi \frac{dB_\nu}{dT}|_{T_{\text{rad}}} \frac{dT_{\text{rad}}}{dT_s} d\nu.
\end{aligned} \tag{16}
$$

315 The minus sign ensures consistency with the sign convention used in most climate studies: OLR
316 typically increases in response to surface warming, so $\lambda_{LW} < 0$. Note that Equation 16 does not
317 contain any terms $\propto d\tau_{\text{surf}}/dT_s$ because the resulting contribution to change in the surface emission
318 decreases with warming at exactly the same rate as the atmospheric emission increases (this can
319 be seen by differentiating Eqn. 14 first before applying the emission-level approximation).

b. Spectral feedback decomposition

321 The net feedback in Equation 16 can be decomposed into multiple spectral regions or bands.
322 The surface term dominates in the window region where $\tau_{\text{surf}} < 1$ and the feedback is primarily
323 a function of surface temperature T_s. The atmospheric emission dominates where $\tau_{\text{surf}} > 1$, and
324 its magnitude primarily depends on the derivative dT_{rad}/dT_s. As we show below, dT_{rad}/dT_s
325 differs depending on the opacity source at a given wavenumber. In this work we only consider
326 Earth's dominant greenhouse gases, CO_2 and H_2O, where H_2O's radiative effect additionally varies
327 between the H_2O bands and the H_2O continuum, so we split the spectral integral into four terms:

$$
\begin{aligned}
-\lambda_{LW} &= \int_{\text{surf}} \pi \frac{dB_\nu}{dT}|_{T_s} e^{-\tau_{\text{surf}}} d\nu + \int_{\text{co}_2} \pi \frac{dB_\nu}{dT}|_{T_{\text{co}_2}} \frac{dT_{\text{co}_2}}{dT_s} d\nu + \\
&\quad \int_{\text{H}_2\text{O}} \pi \frac{dB_\nu}{dT}|_{T_{\text{H}_2\text{O}}} \frac{dT_{\text{H}_2\text{O}}}{dT_s} d\nu + \int_{\text{cnt}} \pi \frac{dB_\nu}{dT}|_{T_{\text{cnt}}} \frac{dT_{\text{cnt}}}{dT_s} d\nu \\
&= -(\lambda_{\text{surf}} + \lambda_{\text{co}_2} + \lambda_{\text{H}_2\text{O}} + \lambda_{\text{cnt}}),
\end{aligned} \tag{17}
$$

328 where T_{co_2}, $T_{\text{H}_2\text{O}}$ and T_{cnt} are the emission temperatures in the CO_2 band, the H_2O band, and the
329 H_2O continuum respectively (the wavenumber range of each integral is discussed in Section 5a).
330 Based on the emitter, we refer to the four feedback terms as the surface feedback (λ_{surf}), the CO_2
331 band feedback (λ_{co_2}), the (non-Simpsonian) H_2O band feedback ($\lambda_{\text{H}_2\text{O}}$), and the H_2O continuum
332 feedback (λ_{cnt}).

333 Our spectral decomposition complements the conventional feedback decomposition which splits
334 λ_{LW} into Planck, Lapse-Rate, and Water Vapor (or Relative Humidity) feedbacks. The surface
335 feedback λ_{surf} measures the OLR increase due to surface warming while keeping the atmosphere
336 fixed. This term is identical to the surface contribution of the Planck feedback, or "surface kernel",
337 in the conventional decomposition (Soden et al. 2008). As for the atmospheric feedback, Equation
338 16 shows that it depends on the *total* derivative of T_{rad}, that is, on dT_{rad}/dT_s. The conventional
339 decomposition can be interpreted as splitting the total derivative dT_{rad}/dT_s up into various partial
340 derivatives (uniform warming versus lapse-rate versus water vapor changes), while using a single,
341 spectrally-averaged T_{rad}. In contrast, our decomposition splits the atmosphere's feedback into
342 three different bands, but still retains the total derivative dT_{rad}/dT_s in each band. In principle
343 our decomposition could be split further to recover the conventional decomposition. That is, one
344 could further decompose dT_{rad}/dT_s in each band into partial derivatives of T_{rad} that correspond to
345 vertically-uniform warming, lapse-rate warming, and water-vapor changes – see Jeevanjee et al.
346 (2021a) for more details. Here, however, we do not pursue this approach because our analytic
347 expressions are general enough to predict T_{rad} and the total derivative dT_{rad}/dT_s.

348 We use relative humidity as the state variable throughout this paper, so the analytic results are
349 compatible with papers that argue for the use of relative humidity in feedback decompositions
350 instead of specific humidity (Held and Shell 2012; Jeevanjee et al. 2021a). In the fixed-RH
351 framework the conventional Water Vapor feedback is replaced by a Relative Humidity feedback,
352 which measures the clear-sky feedback due to RH changes. It is worth noting that the RH feedback
353 is small in individual climate models, and its multi-model mean is close to zero (Zelinka et al.
354 2020). In the derivations below we therefore treat RH as an external parameter whose value is
355 assumed constant under surface warming.

c. Line-by-line calculations

357 To calculate spectral feedbacks numerically we use a 1D line-by-line model, PyRADS (Koll and
358 Cronin 2018). The model's radiative transfer includes HITRAN2016 CO_2 and H_2O absorption data
359 as well as the H_2O component of the MTCKD continuum version 3.2 (Mlawer et al. 2012; Gordon
360 et al. 2017). Calculations cover the spectral range 0.1-2500 cm^{-1} with a resolution of $\Delta \nu = 0.01$
361 cm^{-1}, while the vertical resolution is 50 points in log-pressure. In general the angular distribution

17

of longwave radiation $\cos(\bar{\theta})$ varies in the vertical as well as across wavenumber (Li 2000; Feng and Huang 2019); however, a common approximation is to assume $\cos(\bar{\theta}) = 3/5$ (Elsasser 1942), which is also used here.

The 1D calculations assume the atmosphere's temperature profile follows either a moist adiabat or a power law temperature-pressure profile that is consistent with our bulk lapse rate approximation. In both cases the troposphere is capped by a tropopause at 200 K, while the overlying stratosphere is isothermal at the same temperature. Relative humidity in the troposphere is vertically uniform while the H_2O mass fraction in the stratosphere is set equal to its value at the tropopause. CO_2 is treated as uniformly mixed in the vertical and fixed with respect to surface temperature. Because we are considering a wide range of surface temperatures, across which the tropopause pressure varies substantially, we vary the vertical grid-spacing in PyRADS: for each surface temperature, the model top pressure is set to a slightly lower value than the estimated tropopause pressure based on our bulk lapse rate formulation, which ensures the model's top is always in the stratosphere and the tropopause is well resolved.

The spectrally-resolved feedback is the difference in the spectrally-resolved outgoing longwave flux, OLR_ν, between a base state and a perturbed state with warmed surface and atmosphere,

$$-\lambda_\nu = \frac{OLR_\nu(T_s + \Delta T_s, \vec{T} + \Delta\vec{T}) - OLR_\nu(T_s, \vec{T})}{\Delta T_s}. \tag{18}$$

We use $\Delta T_s = 1$ K, while $\Delta\vec{T}$ denotes the atmospheric temperature perturbation caused by the surface warming ΔT_s. Because relative humidity is kept fixed, the atmospheric warming $\vec{T} + \Delta\vec{T}$ also implies an increase in specific humidity.

Previous work has used various approaches to interpret line-by-line output. Seeley and Jeevanjee (2021) defined CO_2 versus H_2O bands based on the column-integrated, spectrally-smoothed optical thickness of CO_2 and H_2O. However, the behavior of H_2O differs strongly between the H_2O bands and the H_2O continuum, and it is difficult to distinguish these terms based on column-integrated optical thicknesses. For example, the H_2O continuum might have a larger integrated optical thickness at some wavenumber than the H_2O bands, but because continuum absorption decays more rapidly with altitude than band absorption ($\kappa_{cnt} \propto e^*(T)$ versus $\kappa_{H_2O} \propto p$) the emission at the level where $\tau \sim 1$ could still be determined by the H_2O bands.

Instead we first split the net feedback into its contributions from the surface versus atmosphere. The spectrally-resolved surface feedback is the feedback in response to surface-only warming while keeping the atmosphere fixed,

$$-\lambda_{\text{surf}}^{\nu} = \frac{\text{OLR}_{\nu}(T_s + \Delta T_s, \vec{T}) - \text{OLR}_{\nu}(T_s, \vec{T})}{\Delta T_s}. \tag{19}$$

If we integrate $\lambda_{\text{surf}}^{\nu}$ over all wavenumbers we get the surface feedback λ_{surf}, equivalent to the surface kernel of Soden et al. (2008). The atmospheric feedback is equal to the difference between λ_{ν} and $\lambda_{\text{surf}}^{\nu}$,

$$-\lambda_{atm}^{\nu} = \frac{\text{OLR}_{\nu}(T_s, \vec{T} + \Delta\vec{T}) - \text{OLR}_{\nu}(T_s, \vec{T})}{\Delta T_s}. \tag{20}$$

We split λ_{atm}^{ν} into different bands based on the spectrally-resolved emission pressures of CO_2, H_2O, and the H_2O continuum. For each absorber PyRADS computes the optical thickness as a function of pressure and wavenumber, $\tau(p, \nu)$. We define the CO_2 emission pressure as the pressure at which the optical thickness of CO_2 is equal to unity,

$$\tau_{\text{co}_2}(p_{\text{rad}}, \nu) = 1, \tag{21}$$

which can be solved in each wavenumber bin to find $p_{\text{rad}}(\nu)$ (in practice we interpolate to find the pressure at which $\log[\tau] = 0$). The emission pressures of H_2O and the H_2O continuum are determined for each wavenumber bin in the same manner. The CO_2 band feedback λ_{co_2} is then the integral of λ_{atm}^{ν} over all wavenumbers at which CO_2 has the smallest emission pressure, the H_2O band feedback λ_{H_2O} is the integral of λ_{atm}^{ν} over all wavenumbers at which H_2O has the smallest emission pressure, and so on. The spectral decomposition is recomputed each time the atmosphere or surface state is varied, thereby allowing us to capture the state-dependence of the longwave feedback not just due to changes in the atmosphere's and surface's emission but also due to changes in the width of spectral bands. We note that this approach is justified if one emitter clearly dominates the atmosphere's emission at a given wavenumber, such that its emission pressure p_{rad} is much lower than that of any other emitters, but could be misleading if two emitters have very similar emission pressures. In practice, H_2O and CO_2 absorption cross-sections decrease

19

quasi-exponentially away from their band centers (see Section 2), which means the wavenumber
range over which two absorbers can have a similar emission pressure is limited.

4. Emission temperatures

The feedbacks are set by the temperatures at the $\tau = 1$ levels, so we seek analytic expressions for
the emission temperatures T_{co_2}, T_{H_2O} and T_{cnt}. The optical thickness of a generic absorber is

$$\tau = \int \kappa q \frac{dp}{g \cos(\bar{\theta})}, \tag{22}$$

where κ is the absorption cross-section and q is the absorber's mass-specific concentration. We
use this equation to derive expressions for the emission temperatures by first writing the optical
thickness in each band as a function of atmospheric temperature, then inverting these relations to
find the emission temperature at the $\tau = 1$ level.

a. CO$_2$

CO$_2$ is well-mixed in the atmosphere so its mass-specific concentration q_{co_2} is vertically uniform.
As discussed in Section 2, its absorption cross-section depends linearly on pressure due to pressure
broadening and can be written as $\kappa_{co_2}(\nu, p) = \kappa^*_{co_2}(\nu)(p/p_0)$, where $\kappa^*_{co_2}$ captures the wavenumber-
dependence of the CO$_2$ absorption cross-section, $\kappa^*_{co_2} \propto \exp(-|\nu - \nu_0|/l_\nu)$, while p_0 is an reference
pressure. Because we previously chose p_0 to be equal to the dry surface pressure, one can write
$\kappa^*_{co_2}(\nu) \approx \kappa_{co_2}(\nu, p_s)$ (the approximation is due to neglecting the mass contribution of water vapor
to p_s). The optical thickness at a vertical level with temperature and pressure (T, p) is then

$$
\begin{aligned}
\tau_{co_2} &= \int_0^p \kappa^*_{co_2} \left(\frac{p'}{p_s} \right) q_{co_2} \frac{dp'}{g \cos(\bar{\theta})}, \\
&= \frac{\kappa^*_{co_2}}{2g \cos(\bar{\theta}) p_s} q_{co_2} p^2, \\
&= \frac{\kappa^*_{co_2} p_s}{2g \cos(\bar{\theta})} q_{co_2} \left(\frac{p}{p_s} \right)^2 \\
&= \frac{\kappa^*_{co_2} p_s}{2g \cos(\bar{\theta})} q_{co_2} \left(\frac{T}{T_s} \right)^{2/\gamma_{lr}} \\
&\equiv \tau^*_{co_2}(\nu) \, q_{co_2} \times \left(\frac{T}{T_s} \right)^{2/\gamma_{lr}},
\end{aligned} \tag{23}
$$

where the fourth step uses the bulk lapse rate. Note that all spectroscopic parameters as well as p_s and g are combined into a reference optical thickness, $\tau^*_{\text{CO}_2}(\nu)$, which encapsulates how CO_2 absorption varies with respect to wavenumber ν, surface pressure p_s, and gravity g, but which can be treated as constant in response to warming.

b. Non-Simpsonian H_2O

As for CO_2, the absorption cross-section of H_2O scales linearly with pressure and can be written as $\kappa_{\text{H}_2\text{O}}(\nu, p) = \kappa^*_{\text{H}_2\text{O}}(\nu)(p/p_s)$. We use the Clausius-Clapeyron power law approximation to write the saturation specific humidity as $q^* \approx R_d/R_v \times e^*_0/p \times (T/T_0)^{\gamma_{\text{wv}}}$ and the specific humidity as $q = \text{RH} \times q^*$. The optical thickness of H_2O at a level (T, p) is then

$$
\begin{aligned}
\tau_{\text{H}_2\text{O}} &= \int_0^p \kappa^*_{\text{H}_2\text{O}}\left(\frac{p'}{p_s}\right) q \frac{dp'}{g\cos(\bar{\theta})}, \\
&\approx \text{RH}\, \frac{\kappa^*_{\text{H}_2\text{O}} e^*_0}{g\cos(\bar{\theta})} \frac{R_d}{R_v} \times \int_0^p \left(\frac{p'}{p_s}\right)\left(\frac{T'}{T_0}\right)^{\gamma_{\text{wv}}} \frac{dp'}{p'} \\
&= \text{RH}\, \frac{\kappa^*_{\text{H}_2\text{O}} e^*_0}{g\cos(\bar{\theta})} \frac{R_d}{R_v} \times \int_0^T \left(\frac{T'}{T_s}\right)^{1/\gamma_{\text{lr}}} \left(\frac{T'}{T_0}\right)^{\gamma_{\text{wv}}} \frac{1}{\gamma_{\text{lr}}} \frac{dT'}{T'} \\
&= \text{RH}\, \frac{\kappa^*_{\text{H}_2\text{O}} e^*_0}{g\cos(\bar{\theta})} \frac{R_d}{R_v} \frac{1}{\gamma_{\text{lr}}} \left(\frac{T_0}{T_s}\right)^{1/\gamma_{\text{lr}}} \times \int_0^T \left(\frac{T'}{T_0}\right)^{\gamma_{\text{wv}}+\frac{1}{\gamma_{\text{lr}}}} \frac{dT'}{T'} \\
&= \text{RH}\, \frac{\kappa^*_{\text{H}_2\text{O}} e^*_0}{g\cos(\bar{\theta})} \frac{R_d}{R_v} \frac{1}{1+\gamma_{\text{wv}}\gamma_{\text{lr}}} \times \left(\frac{T}{T_0}\right)^{\frac{1+\gamma_{\text{wv}}\gamma_{\text{lr}}}{\gamma_{\text{lr}}}} \left(\frac{T_0}{T_s}\right)^{1/\gamma_{\text{lr}}} \\
&\equiv \text{RH}\, \tau^*_{\text{H}_2\text{O}}(\nu) \frac{1}{1+\gamma_{\text{wv}}\gamma_{\text{lr}}} \times \left(\frac{T}{T_0}\right)^{\frac{1+\gamma_{\text{wv}}\gamma_{\text{lr}}}{\gamma_{\text{lr}}}} \left(\frac{T_0}{T_s}\right)^{1/\gamma_{\text{lr}}}.
\end{aligned}
\tag{24}
$$

where the second step uses the Clausius-Clapeyron power law and also replaces the water vapor concentration in the stratosphere with the water vapor concentration of a moist adiabat that extends all the way to the top-of-atmosphere. We again define a reference optical thickness, $\tau^*_{\text{H}_2\text{O}}(\nu)$, which encapsulates how H_2O band absorption varies with respect to wavenumber ν, and gravity g, but which is independent of temperature.

c. H_2O Continuum

Absorption by the H_2O continuum strengthens in response to increasing water vapor concentrations and weakens in response to warming, $\kappa_{\text{H}_2\text{O,cnt}} = \kappa_{\text{cnt}} \times \text{RH}\, e^*(T)/e^*(T_0) \times (T/T_0)^{-a}$. The

21

optical thickness of the continuum is then

$$
\begin{aligned}
\tau_{\text{cnt}} &= \text{RH} \int_0^p \kappa_{\text{cnt}} \frac{e^*(T')}{e^*(T_0)} \left(\frac{T'}{T_0}\right)^{-a} q \frac{dp'}{g\cos(\bar{\theta})}, \\
&\approx \text{RH}^2 \frac{\kappa_{\text{cnt}} e_0^*}{g\cos(\bar{\theta})} \frac{R_d}{R_v} \times \int_0^T \left(\frac{T'}{T_0}\right)^{2\gamma_{\text{wv}}-a} \frac{dp'}{p}, \\
&= \text{RH}^2 \frac{\kappa_{\text{cnt}} e_0^*}{g\cos(\bar{\theta})} \frac{R_d}{R_v} \times \int_0^T \left(\frac{T'}{T_0}\right)^{2\gamma_{\text{wv}}-a} \frac{1}{\gamma_{\text{lr}}} \frac{dT'}{T'}, \\
&= \text{RH}^2 \frac{\kappa_{\text{cnt}} e_0^*}{g\cos(\bar{\theta})} \frac{R_d}{R_v} \frac{1}{(2\gamma_{\text{wv}}-a)\gamma_{\text{lr}}} \times \left(\frac{T}{T_0}\right)^{2\gamma_{\text{wv}}-a}, \\
&\equiv \text{RH}^2 \, \tau_{\text{cnt}}^* \frac{1}{(2\gamma_{\text{wv}}-a)\gamma_{\text{lr}}} \times \left(\frac{T}{T_0}\right)^{2\gamma_{\text{wv}}-a},
\end{aligned}
\tag{25}
$$

where the second and third steps make the same assumptions as the derivation for the H_2O band. Here the reference optical thickness, τ_{cnt}^* encapsulates how the H_2O self-continuum varies with respect to gravity g but has no dependence on wavenumber or temperature.

d. Emission temperatures

By setting $\tau = 1$ and inverting the above relations, we arrive at the emission temperatures in the CO_2 band, the H_2O band and the H_2O self-continuum:

$$
T_{\text{co}_2} = T_s \left(\frac{1}{\tau_{\text{co}_2}^*(\nu) q_{\text{co}_2}}\right)^{\gamma_{\text{lr}}/2}
\tag{26a}
$$

$$
T_{H_2O} = T_0 \left(\frac{1+\gamma_{\text{wv}}\gamma_{\text{lr}}}{\tau_{H_2O}^*(\nu)\text{RH}}\right)^{\frac{\gamma_{\text{lr}}}{1+\gamma_{\text{wv}}\gamma lr}} \left(\frac{T_s}{T_0}\right)^{\frac{1}{1+\gamma_{\text{wv}}\gamma lr}}
\tag{26b}
$$

$$
T_{\text{cnt}} = T_0 \left(\frac{(2\gamma_{\text{wv}}-a)\gamma_{\text{lr}}}{\tau_{\text{cnt}}^*\text{RH}^2}\right)^{\frac{1}{2\gamma_{\text{wv}}-a}}.
\tag{26c}
$$

To interpret these emission temperatures, consider whether a given emitter stabilizes or destabilizes Earth's climate. For CO_2 it is easy to see that the feedback is always stabilizing. Ignoring lapse rate changes we have $T_{\text{co}_2} \propto T_s$, so $dT_{\text{co}_2}/dT_s > 0$. More intuitively, the optical thickness of

22

CO$_2$ can be written as

$$\tau_{\text{co}_2} \quad \propto \quad \left(\frac{T}{T_s}\right)^{2/\gamma_{\text{lr}}} = \left(\frac{p}{p_s}\right)^2. \tag{27}$$

The emission level of CO$_2$ is therefore a fixed function of pressure at a given atmospheric CO$_2$ concentration. Given that the atmosphere's temperature at a fixed pressure level always increases in response to surface warming, T_{co_2} also has to increase under warming. This effect can be thought of as a spectral radiator fin, and is also valid if the lapse rate γ_{lr} varies under surface warming. It implies that even if the atmosphere stops emitting more at all other wavenumbers, so $dT_{\text{rad}}/dT_s = 0$ outside the CO$_2$ band, the presence of CO$_2$ still allows the atmosphere to shed more energy to space in response to surface warming (Seeley and Jeevanjee 2021).

Next, our expressions suggest that the feedback from H$_2$O is small and, to first order, might be negligible. Equation 26b shows $T_{\text{H}_2\text{O}} \propto T_s^{1/(1+\gamma_{\text{wv}}\gamma_{\text{lr}})}$, where representative values for Earth's tropics are $\gamma_{\text{wv}} \sim 20$ and $\gamma_{\text{lr}} \sim 1/7$, so the H$_2$O emission temperature only depends weakly on surface temperature, $T_{\text{H}_2\text{O}} \propto T_s^{1/4}$. This small exponent is closely related to Simpson's "paradox" (Ingram 2010) or Simpson's "law" (Jeevanjee et al. 2021a), which state that $T_{\text{H}_2\text{O}}$ is approximately independent of surface temperature. In the limit $\gamma_{\text{wv}}\gamma_{\text{lr}} = d\ln e^*/d\ln p \gg 1$, that is, if water vapor increases much faster in the vertical than the total atmospheric mass, then

$$T_{\text{H}_2\text{O}} \quad \approx \quad T_0 \left(\frac{\gamma_{\text{wv}}\gamma_{\text{lr}}}{\tau_{\text{H}_2\text{O}}^*(\nu)RH}\right)^{\frac{1}{\gamma_{\text{wv}}}}, \tag{28}$$

and $T_{\text{H}_2\text{O}}$ ceases to depend on T_s. If the lapse rate is also independent of T_s we recover Simpon's law:

$$\frac{dT_{\text{H}_2\text{O}}}{dT_s} \quad \approx \quad 0. \tag{29}$$

In reality, however, water vapor dominates much of the spectrum so even minor deviations from Simpson's law can have a notable impact on the longwave feedback. Deviations arise because the H$_2$O optical thickness is sensitive to pressure broadening and because changes in γ_{lr} modify the total water vapor path inside the atmospheric column. For present-day Earth the net impact of these

23

changes is to increase the H_2O emission temperature under surface warming: since $T_{H_2O} \propto T_s^{1/4}$, it follows that $dT_{H_2O}/dT_s > 0$, which means the H_2O bands tend to stabilize Earth's climate.

Finally, T_{cnt} has no direct dependence on surface temperature, but is sensitive to lapse rate changes. If we take the continuum's emission temperature (Eqn. 26c), and assume that the direct temperature-dependence of the continuum $a \sim 7$ is much smaller than its temperature-dependence due to the Clausius-Clapeyron relation, $2\gamma_{wv} \sim 40$, we have

$$T_{cnt} \quad \propto \quad T_0 \times [\gamma_{lr}]^{1/(2\gamma_{wv})}. \tag{30}$$

Because the lapse rate γ_{lr} decreases under surface warming we have $dT_{cnt}/dT_s = dT_{cnt}/d\gamma_{lr} \times d\gamma_{lr}/dT_s < 0$. Physically, this effect can be understood by considering the impact of γ_{lr} on the atmosphere's total water vapor path. If one decreases the lapse rate γ_{lr} while keeping T_s fixed, the atmospheric column warms and thus can store more water vapor. To still maintain an optical thickness of unity then requires that the continuum's emission level moves to colder temperatures. Our expressions thus predict that the H_2O continuum gives rise to a destabilizing feedback.

e. Comparison against LBL calculations

Equations 26a - 26c predict how Earth's emission temperature varies in response to changes in T_s, q_{co_2}, γ_{lr} and RH. To test these equations we perform four sets of numerical experiments with PyRADS in which we variously change T_s, q_{co_2}, γ_{lr}, and RH while holding the other parameters fixed. The default values are $T_s = 290$ K, 400 ppm of CO_2, $\gamma_{lr} = 2/7$, and RH = 0.8. To match our underlying assumptions we assume a bulk tropospheric lapse rate, so $T = T_s(p/p_s)^{\gamma_{lr}}$, which means the temperature profile differs from an adiabat if $\gamma_{lr} < 2/7$. The troposphere is capped by an isothermal stratosphere which is kept fixed at $T_{strat} = 200$ K. Note that in Equations 26a - 26c the dependence on wavenumber only enters through the reference optical thicknesses $\tau_{co_2}^*$, $\tau_{H_2O}^*$, and τ_{cnt}^*, which are evaluated using the cross-sections from Section 2. Because the cross-sections were fit independently, the analytic T_{rad} expressions do not contain any free tuning parameters.

To compare the analytic results against line-by-line calculations we first numerically compute the top-of-atmosphere spectral flux OLR_ν for a given set of $(T_s, q_{co_2}, \gamma_{lr}, RH)$. We then smooth OLR_ν with a median filter of width 50 cm^{-1}, before inverting it using the Planck function to find the

24

atmosphere's emission temperature (also known as brightness temperature) at a given wavenumber. Finally, we combine our analytic expressions into a single emission temperature via

$$T_{\text{rad}} \quad = \quad \max \left[T_{\text{strat}}, \min \left[T_s, T_{\text{co}_2}, T_{\text{H}_2\text{O}}, T_{\text{cnt}} \right] \right], \tag{31}$$

to compare directly with temperatures from line-by-line calculations.

Figure 4 demonstrates that the analytic results compare favorably against numerical calculations. Even though the analytic T_{rad} shapes are idealized compared to the numerical calculations, the overall response of T_{rad} to perturbations is captured well. First, increasing CO_2 concentration lowers T_{rad} around 667 cm^{-1}, which corresponds to the wings of the CO_2 band. This is simply a spectrally resolved view of how increasing CO_2 acts as a radiative forcing (Jeevanjee et al. 2021b). Second, warming the surface while keeping all other parameters fixed has multiple effects. The main impact is to increase the emission temperature in the window region between ~ 800 and 1200 cm^{-1}. In addition there are secondary impacts: surface warming also shrinks the width of the CO_2 band and slightly increases the emission temperature in the H_2O bands below 600 cm^{-1} and above 1300 cm^{-1} (this latter effect is hard to see in Figure 4). The increased emission in the H_2O bands shows that Simpson's law in Equation 29 is not exact, an effect that is captured by our analytic expressions. Third, reducing the lapse rate γ_{lr} preserves the width of the CO_2 band, but it flattens the steepness of its slopes and increases the emission temperature in the center of the band. In the H_2O bands, a smaller γ_{lr} while keeping T_s fixed also leads to a non-Simpsonian increase of the emission temperature in the H_2O bands. In contrast to the H_2O bands, the emission temperature of the H_2O continuum around 1000 cm^{-1} decreases as γ_{lr} is reduced. As discussed above, this is because the atmospheric water path increases with a smaller γ_{lr}, which reduces T_{cnt}. The feedback of the H_2O continuum therefore has the opposite sign as the H_2O bands, in line with the analytic results. Finally, reducing the relative humidity increases T_{rad} in all regions dominated by water vapor, both in the H_2O bands below 600 cm^{-1}/above 1300 cm^{-1} and in the H_2O continuum around 1000 cm^{-1}, while the CO_2 band is unaffected.

Overall, Figure 4 underlines that comparatively simple physics is sufficient to explain the spectrally-resolved response of T_{rad} to different climate perturbations. To connect Figure 4 back to the total clear-sky longwave feedback we only need to consider how these changes in T_{rad} play
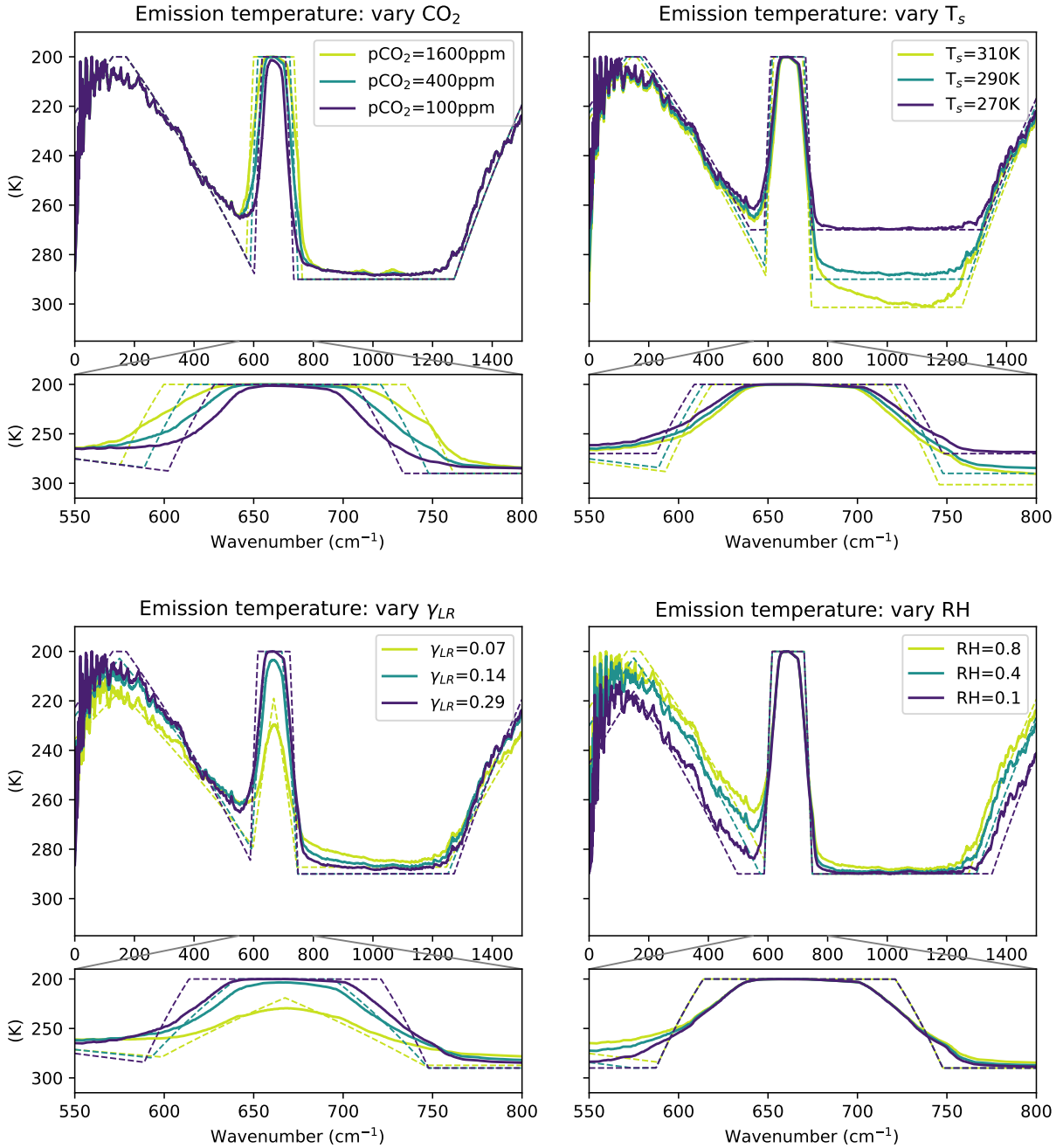
25

FIG. 4. Analytic emission temperatures (dashed), compared against numerical line-by-line results smoothed with a median filter of width 50 cm^{-1}. Large rows show the entire infrared spectrum, small rows are zoomed in on the CO_2 band. The y-axes are flipped so that emission temperature decreases going up, the same way temperature decreases with altitude in Earth's atmosphere.

₅₃₃ out once we average them into spectral bands, and how multiple bands add up to determine the net
₅₃₄ longwave feedback.

5. Analytic Feedbacks

₅₃₆ Having derived expressions for the emission temperature in different parts of the LW spectrum,
₅₃₇ and verified these expressions against line-by-line calculations, we can now derive analytic expres-
₅₃₈ sions for the four spectral feedbacks: λ_{surf}, $\lambda_{\mathrm{co_2}}$, $\lambda_{\mathrm{H_2O}}$ and λ_{cnt}. Above each spectral feedback was
₅₃₉ defined as an integral over a wavenumber range (Eqn. 17), but the wavenumber ranges were not
₅₄₀ further specified. We therefore first define and estimate the width of the different spectral bands.

₅₄₁ *a. Band widths*
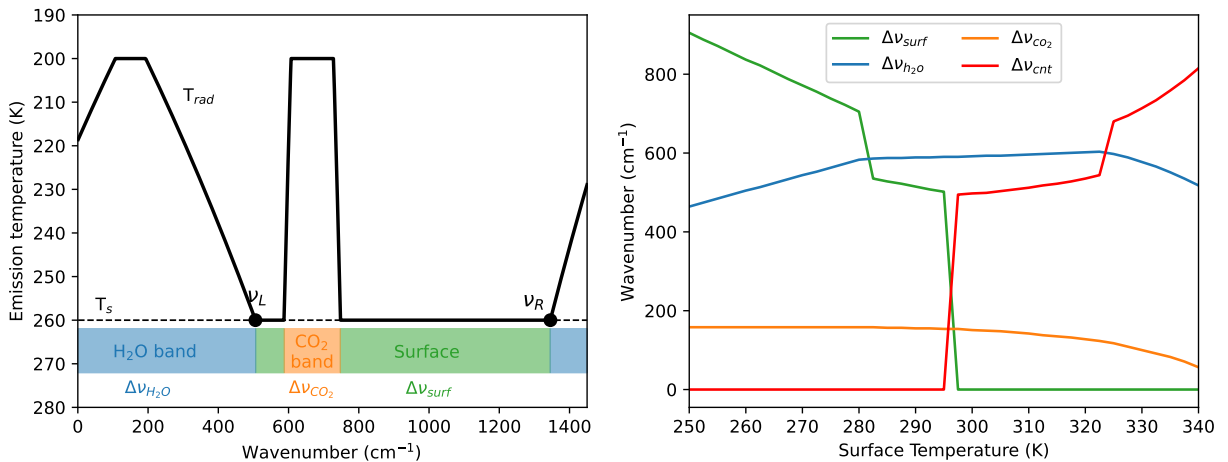
₅₄₂ FIG. 5. Illustration of spectral band widths. The emission temperature is equal to the emission temperature of
₅₄₃ whichever emitter is coldest, $T_{\mathrm{rad}} = \min[T_{\mathrm{co_2}}, T_{\mathrm{H_2O}}, T_{\mathrm{cnt}}, T_s]$, or the stratospheric temperature. Left: Lines show
₅₄₄ the analytic T_{rad} (solid) and surface temperature T_s (dashed), while colored regions illustrate which emitters
₅₄₅ dominate in which band. The calculation shown uses T_s=260 K, RH = 0.8, and 400ppm of CO_2. Right:
₅₄₆ Band widths as a function of surface temperature, numerically calculated based on our emission temperature
₅₄₇ expressions. Here $\Delta\nu_{\mathrm{H_2O}}$ refers only to the rotational band at wavenumbers lower than 1000 cm^{-1}. The jumps at
₅₄₈ ~280 K, ~295 K and ~325 K occur when the H_2O band starts intersecting the CO_2 band; when the continuum
₅₄₉ becomes opaque; and when the continuum becomes opaque on the left side of the CO_2 band, at wavenumbers
₅₅₀ less than about 600 cm^{-1}, respectively.

We define an absorption band as the spectral range in which a given absorber has the coldest emission temperature compared to all other absorbers (this is equivalent to the highest-altitude emission level), and thus dominates the column's emission to space. For example, the CO_2 band is defined as all wavenumbers in which $T_{co_2} < \min[T_{H_2O}, T_{cnt}, T_s]$, as illustrated in Figure 5a. The width of the CO_2 band can then be computed from the two wavenumbers ν^{edge} which define the edges of the CO_2 band, which is where the emission temperature of CO_2 is equal to the emission temperatures of its neighboring absorbers: $T_{co_2}(\nu^{edge}) = \min[T_{H_2O}(\nu^{edge}), T_{cnt}, T_s]$.

1) CO_2 BAND WIDTH

To estimate the width of the CO_2 band we consider three situations: (1) the CO_2 concentration q_{co_2} is so low that even in the center of the CO_2 band the optical thickness is less than one; (2) a dry atmosphere in which there is no overlap between CO_2 and H_2O bands; and (3) a moist atmosphere in which there is some overlap between CO_2 and H_2O.

First, at very low CO_2 concentrations the band width of CO_2 is simply equal to zero. From the optical thickness of CO_2 (Eqn. 23), the column-integrated optical thickness in the middle of the CO_2 band is equal to $\tau_{co_2}(\nu_0, T_s) = q_{co_2}\tau_{co_2}^*(\nu_0)$ so this occurs when

$$\Delta\nu_{co_2} \quad = 0, \quad \text{if } q_{co_2}\tau_{co_2}^*(\nu_0) < 1. \tag{32}$$

As a representative value, we evaluate $\tau_{co_2}^*(\nu_0)$ using $\kappa_0 = 500$ m^2 kg^{-1} from Section 2c. We find that the middle of the CO_2 band becomes optically thick above a CO_2 concentration of ~ 0.2 ppm. Note this value is only approximate, as our idealized band model deviates from real CO_2 absorption cross-section in the middle of the CO_2 band (see Fig. 3).

Second, at non-negligible CO_2 concentrations and low water vapor concentrations, CO_2-H_2O overlap is negligible. Physically, this occurs either when the surface temperature is cold or the relative humidity is low; for simplicity we refer to this as the "cold" regime. In this regime the edge of the CO_2 band can be defined as the wavenumber ν^{cold} at which T_{co_2} intersects with the surface temperature T_s, $T_{co_2}(\nu^{cold}) = T_s$. The emission temperature of CO_2 is equal to $T_{co_2} = T_s \times (\tau_{co_2}^* q_{co_2})^{-\gamma_{lr}/2}$ (Eqn. 26a), while our model of CO_2 spectroscopy states $\tau_{co_2}(\nu)^* \propto \exp(-|\nu - \nu_0|/l_\nu)$

28

(Eqn. 11). Combining the two equations yields

$$\nu^{cold} \quad = \quad \nu_0 \pm l_\nu \log\left(q_{\text{co}_2} \tau^*_{\text{co}_2}(\nu_0)\right), \tag{33}$$

where $\tau^*_{\text{co}_2}(\nu_0) = \kappa_0(\nu_0) p_s / (2g)$ is the reference optical thickness in the center of the CO_2 band. The overall width of the CO_2 band in the cold regime is therefore

$$\Delta \nu^{cold}_{\text{co}_2} \quad = \quad 2 l_\nu \log\left(q_{\text{co}_2} \tau^*_{\text{co}_2}(\nu_0)\right). \tag{34}$$

To estimate the order of magnitude of $\Delta \nu^{cold}_{\text{co}_2}$ we again use $\kappa_0 = 500$ m^2 kg^{-1} and a q_{co_2} that corresponds to 400ppm of CO_2. The optical thickness in the center of the CO_2 band is $\tau^*_{\text{co}_2}(\nu_0) \sim$ 2600. This large optical thickness decreases exponentially with wavenumber away from ν_0, so that $T_{\text{co}_2} = T_s$ only ~ 80 cm^{-1} away from ν_0. Because CO_2's band shape is symmetric about ν_0, the present-day CO_2 band width is thus roughly 160 cm^{-1}.

Third, at high water vapor concentrations, surface emission is replaced by H_2O emission. Physically, this occurs either when the surface temperature is hot and/or relative humidity is high; for simplicity we refer to this as the "hot" regime. In this regime we solve the CO_2 band width as $T_{\text{co}_2}(\nu^{hot}) = T_{H_2O}(\nu^{hot})$. Because the CO_2 band decays much faster with wavenumber away from its band center than the H_2O band does ($l_\nu \sim 10$ cm^{-1} versus $l_{\text{rot}} \sim 55$ cm^{-1}; see Table 1) we further approximate T_{H_2O} as constant across the CO_2 band and equal to its value in the CO_2 band center $T_{H_2O}(\nu) \approx T_{H_2O}(\nu_0)$. Combining the emission temperature of CO_2 (Eqn. 26a) with our model of CO_2 spectroscopy (Eqn. 11),

$$\nu^{hot} \quad = \quad \nu_0 \pm l_\nu \log\left[q_{\text{co}_2} \tau^*_{\text{co}_2}(\nu_0) \left(\frac{T_{H_2O}(\nu_0)}{T_s} \right)^{\frac{2}{\gamma_{\text{lr}}}} \right], \tag{35}$$

where the emission temperature of H_2O can be evaluated using Eqn. 26b. Physically speaking, the H_2O emission temperature is colder than the surface, $T_{H_2O}(\nu_0)/T_s < 1$, so our model correctly captures the fact that H_2O-CO_2 overlap decreases the width of the CO_2 band. Taking into account

29

all three regimes, the overall width of the CO_2 band is therefore

$$\Delta\nu_{\mathrm{co_2}} = \begin{cases} 0, & \text{if } q_{\mathrm{co_2}}\tau^*_{\mathrm{co_2}}(\nu_0) < 1 \\ 2\times\min\left(\nu^{hot}-\nu_0, \nu^{cold}-\nu_0\right), & \text{if } q_{\mathrm{co_2}}\tau^*_{\mathrm{co_2}}(\nu_0) \geq 1. \end{cases} \tag{36}$$

2) H_2O BAND WIDTH

To determine the width of the H_2O band the potential overlap with CO_2 matters less because the CO_2 band is too narrow to block a significant portion of the emission by H_2O (at present-day CO_2 concentrations). However, at high water vapor concentrations, competition between the H_2O bands and the H_2O continuum becomes important, so we again consider a "cold" and a "hot" regime. At low water vapor concentrations (physically, at cold temperature or low relative humidity) continuum absorption is negligible and we solve $T_{H_2O}(\nu^{cold}) = T_s$. Combining the emission temperature of H_2O (Eqn. 26b) with our H_2O band model (Eqn. 12), this leads to

$$\nu_L^{cold} = \nu_{\mathrm{rot}} + l_{\mathrm{rot}}\log\left(\frac{\mathrm{RH}\tau^*_{\mathrm{rot}}(\nu_{\mathrm{rot}})}{1+\gamma_{\mathrm{wv}}\gamma_{\mathrm{lr}}}\left(\frac{T_s}{T_0}\right)^{\gamma_{\mathrm{wv}}}\right), \tag{37a}$$

$$\nu_R^{cold} = \nu_{\mathrm{v-r}} - l_{\mathrm{v-r}}\log\left(\frac{\mathrm{RH}\tau^*_{\mathrm{v-r}}(\nu_{\mathrm{v-r}})}{1+\gamma_{\mathrm{wv}}\gamma_{\mathrm{lr}}}\left(\frac{T_s}{T_0}\right)^{\gamma_{\mathrm{wv}}}\right), \tag{37b}$$

where ν_L is the left edge of the window below ~ 1000 cm^{-1}, and ν_R is the right edge of the window above ~ 1000 cm^{-1} (see Figure 5). The two H_2O bands have different spectral slopes, and subscript "rot" denotes quantities that are related to the rotational H_2O band at wavenumbers below 1000 cm^{-1} while subscript "v-r" denotes quantities related to the vibrational-rotational H_2O band at wavenumbers above 1000 cm^{-1} (see Section 2). At high water vapor concentrations, the continuum cuts off emission from the surface so the H_2O band edge ν^{hot} is determined by $T_{H_2O}(\nu^{hot}) = T_{\mathrm{cnt}}$. Using the emission temperature of H_2O (Eqn. 26b) and our H_2O band model, we find

$$\nu_L^{hot} = \nu_{\mathrm{rot}} + l_{\mathrm{rot}}\log\left[\frac{\mathrm{RH}\tau^*_{\mathrm{rot}}(\nu_{\mathrm{rot}})}{1+\gamma_{\mathrm{wv}}\gamma_{\mathrm{lr}}}\left(\frac{T_0}{T_s}\right)^{1/\gamma_{\mathrm{lr}}}\left(\frac{T_{\mathrm{cnt}}}{T_0}\right)^{\frac{1+\gamma_{\mathrm{wv}}\gamma_{\mathrm{lr}}}{\gamma_{\mathrm{lr}}}}\right], \tag{38a}$$

$$\nu_R^{hot} = \nu_{\mathrm{v-r}} - l_{\mathrm{v-r}}\log\left[\frac{\mathrm{RH}\tau^*_{\mathrm{v-r}}(\nu_{\mathrm{v-r}})}{1+\gamma_{\mathrm{wv}}\gamma_{\mathrm{lr}}}\left(\frac{T_0}{T_s}\right)^{1/\gamma_{\mathrm{lr}}}\left(\frac{T_{\mathrm{cnt}}}{T_0}\right)^{\frac{1+\gamma_{\mathrm{wv}}\gamma_{\mathrm{lr}}}{\gamma_{\mathrm{lr}}}}\right], \tag{38b}$$

30

where the continuum emission temperature is given by Eqn. 26c. Combining both regimes, the window width due to H_2O absorption is therefore

$$
\begin{aligned}
\Delta \nu_{\text{surf}}(T_s, \text{RH}, \gamma_{\text{lr}}) &= \nu_R - \nu_L \\
&= \max(\nu_R^{cold}, \nu_R^{hot}) - \min(\nu_L^{cold}, \nu_L^{hot}).
\end{aligned} \tag{39}
$$

Similar to the CO_2 band width, Equations 37 and 38 become invalid at very low RH or T_s because in those situations H_2O ceases to be optically thick at all wavenumbers (mathematically, this happens when RH or T_s become small enough that the logarithms in Eqns. 37 and 38 change sign). We do not consider the limit $\text{RH} \to 0$ in this paper, but care should be taken when applying our results to extremely dry or cold atmospheres.

Finally, our feedback expression for the H_2O band feedback requires us to separately specify the width of the rotational H_2O band below 1000 cm^{-1}. This width can be estimated by assuming that the rotational band always extends from 0 cm^{-1} to the left edge of the window region ν_L (see Figure 5). Doing so presumes that H_2O is always optically thick at low wavenumbers around $\nu = 0$ cm^{-1}. While this assumption again breaks down in very cold or dry climates (the maximum absorption in the rotational band occurs around $\nu \sim 150$ cm^{-1}, not 0 cm^{-1}, so low wavenumbers could become optically thin even if the band center is still optically thick), in those climates the H_2O band feedback becomes negligible relative to the surface anyway. The width of the rotational H_2O band is then

$$
\Delta \nu_{H_2O}(T_s, \text{RH}, \gamma_{\text{lr}}) \approx \nu_L - 0 = \min(\nu_L^{cold}, \nu_L^{hot}), \tag{40}
$$

where the wavenumber ν_L denotes the left edge of the surface window (see above), as well as the right edge of the rotational H_2O band.

b. Surface Feedback

The surface feedback is given by

$$
-\lambda_{\text{surf}} = \int_{\text{surf}} \pi \frac{dB_\nu}{dT}|_{T_s} e^{-\tau_{\text{surf}}} d\nu. \tag{41}
$$

31

The column-integrated optical thickness at a single frequency is the sum over all absorbers at that frequency, $\tau_{\text{surf}}(\nu) = \tau_{H_2O}(\nu) + \tau_{co_2}(\nu) + \tau_{\text{cnt}}$. However, the optical thickness of H_2O and CO_2 drops off exponentially as a function of wavenumber away from their band centers. Thus most frequencies are either so optically thick with respect to H_2O and CO_2 that all surface radiation is absorbed by the atmosphere (and hence does not contribute to the surface feedback), or so optically thin that we can ignore H_2O and CO_2. Inside the window we therefore only consider absorption by the grey continuum, $\tau_{\text{surf}} \approx \tau_{\text{cnt}}$, while the H_2O and CO_2 bands primarily set the width of the window.

To determine the width of the window we first consider an atmosphere without CO_2. As discussed above, in this case the window region is set the H_2O bands, with ν_L denoting the left window edge around ~ 700 cm^{-1} and ν_R the right window edge around ~ 1200 cm^{-1}. The H_2O continuum is grey and so can be taken out of the spectral integral,

$$-\lambda_{\text{surf}} \quad \approx \quad e^{-\tau_{\text{cnt}}(T_s)} \int_{\nu_L}^{\nu_R} \pi \frac{dB_\nu}{dT}|_{T_s} d\nu.$$

We approximate the integral by treating the Planck function derivative as constant with respect to wavenumber, evaluated at the central wavenumber $\tilde{\nu}$ of the window region, so $\int dB_\nu/dT d\nu \propto dB_{\tilde{\nu}}/dT \times \Delta\nu$. In reality the Planck derivative is not constant with wavenumber, so our approximation should only be treated as a scaling which we account for by including a scaling constant c_{surf}. The magnitude of c_{surf} is further discussed below. The result is

$$-\lambda_{\text{surf}} \quad \approx \quad c_{\text{surf}} \times \pi \frac{dB_{\tilde{\nu}}}{dT}|_{T_s} \, e^{-\tau_{\text{cnt}}(T_s)} \, \Delta\nu_{\text{surf}},$$

where $\Delta\nu_{\text{surf}} = \nu_R - \nu_L$ is the window region width due to H_2O band absorption (see Eqn. 39), and we determine the central wavenumber of the window as $\tilde{\nu} = (\nu_R + \nu_L)/2$.

Next, we add the effect of CO_2-surface spectral blocking. Even if the atmosphere contained no water vapor whatsoever, part of the surface's emission would still be absorbed by CO_2 and thus have no effect on the TOA feedback. We account for the potential overlap between the surface and CO_2 by simply subtracting the CO_2 band width from the H_2O-only window width,

$$\Delta\tilde{\nu}_{\text{surf}} \quad = \quad \max \left[0, \Delta\nu_{\text{surf}}(T_s, \text{RH}, \gamma_{\text{lr}}) - \Delta\nu_{co_2}(q_{co_2}) \right], \tag{42}$$

where $\Delta \nu_{CO_2}$ is defined above (Eqn. 36) and the tilde distinguishes the window width here from the H$_2$O-only window width. Our final expression for the surface feedback is thus

$$-\lambda_{\text{surf}} \quad \approx \quad c_{\text{surf}} \times \pi \frac{dB_{\tilde{\nu}}}{dT}|_{T_s} \; e^{-\tau_{\text{cnt}}(T_s)} \; \Delta \tilde{\nu}_{\text{surf}}. \tag{43}$$

c. H$_2$O band feedback

The H$_2$O band feedback is given by

$$-\lambda_{H_2O} \quad = \quad \int_{H_2O} \pi \frac{dB_\nu}{dT}|_{T_{H_2O}} \frac{dT_{H_2O}}{dT s} d\nu. \tag{44}$$

As sketched in Figure 5, we consider the rotational H$_2$O band as ranging from $\nu \approx 0$ to the left edge of the window, ν_L. We do not consider the potential feedback from the vibration-rotation band at wavenumbers higher than ~ 1250 cm^{-1} and, for purposes of the H$_2$O band feedback, also ignore CO$_2$-H$_2$O overlap effects.

The derivative of T_{H_2O} can be solved analytically. If water vapor behaved strictly according to Simpson's law then $dT_{H_2O}/dT_s = 0$ and the H$_2$O band feedback would be zero. Simpson's law is only an approximation, however, so

$$
\begin{aligned}
\frac{dT_{H_2O}}{dT_s} \quad &= \quad \frac{\partial T_{H_2O}}{\partial T_s} + \frac{\partial T_{H_2O}}{\partial \gamma_{\text{lr}}} \frac{d\gamma_{\text{lr}}}{dT_s} \\
&= \quad \frac{1}{1 + \gamma_{\text{wv}}\gamma_{\text{lr}}} \frac{T_{H_2O}}{T_s} + \\
&\quad \frac{\gamma_{\text{wv}}\gamma_{\text{lr}} - \gamma_{\text{wv}} \log\left(\frac{T_s}{T_0}\right) + \log\left(\frac{1 + \gamma_{\text{wv}}\gamma_{\text{lr}}}{\text{RH}\tau_0^*}\right)}{(1 + \gamma_{\text{wv}}\gamma_{\text{lr}})^2} T_{H_2O} \times \frac{d\gamma_{\text{lr}}}{dT_s}.
\end{aligned} \tag{45}
$$

One could also explicitly write out the lapse rate derivative $d\gamma_{\text{lr}}/dT_s$, but the resulting expressions are long and do not lead to additional physical insight, so in practice we evaluate $d\gamma_{\text{lr}}/dT_s$ numerically. To estimate a typical value for dT_{H_2O}/dT_s we ignore lapse rate changes, that is, the second term in Equation 45. Assuming values representative of Earth's tropics, $1 + \gamma_{\text{wv}}\gamma_{\text{lr}} = 1 + 1/7 \times 20 \sim 4$, and representative temperatures $T_{H_2O} \sim 240$ K (see Figure 4) and $T_s \sim 300$ K, a characteristic value

33

for dT_{H_2O}/dT_s is thus

$$\frac{dT_{H_2O}}{dT_s} \quad \sim \quad \frac{1}{4} \times \frac{240}{300} = \frac{1}{5}, \tag{46}$$

in line with the numerical results of Jeevanjee et al. (2021a).

Next, we treat the H_2O band feedback similar to the surface feedback. We assume the integrand of the spectral feedback integral is approximately constant with respect to wavenumber, and equal to its value at a central frequency $\tilde{\nu}$. The feedback is then

$$\begin{aligned} -\lambda_{H_2O} &= \int_0^{\nu_L} \pi \frac{dB_\nu}{dT}\big|_{T_{H_2O}} \frac{dT_{H_2O}}{dT s} d\nu \\ &\approx c_{H_2O} \times \pi \left.\frac{dB_{\tilde{\nu}}}{dT}\right|_{T_{H_2O}(\tilde{\nu})} \times \left.\frac{dT_{H_2O}}{dT s}\right|_{\tilde{\nu}} \times \Delta\nu_{H_2O}, \end{aligned} \tag{47}$$

where $\Delta\nu_{H_2O} = \nu_L$ is the width of the H_2O band, $\tilde{\nu} = \nu_L/2$ is the central wavenumber of the H_2O band, and c_{H_2O} is again a scaling constant to account for the fact that we are replacing a spectral integral with simple multiplication.

d. H_2O continuum feedback

The H_2O continuum feedback is

$$-\lambda_{cnt} = \int_{cnt} \pi \frac{dB_\nu}{dT}\big|_{T_{cnt}} \frac{dT_{cnt}}{dT_s} d\nu. \tag{48}$$

We apply the same logic as for the surface and H_2O band feedbacks. The derivative dT_{cnt}/dT_s can be solved for analytically: T_{cnt} has no dependence on T_s other than through lapse rate changes, so

$$\begin{aligned} \frac{dT_{cnt}}{dT_s} &= \frac{\partial T_{cnt}}{\partial \gamma_{lr}} \frac{d\gamma_{lr}}{dT_s} \\ &= \frac{T_{cnt}}{\gamma_{lr}(2\gamma_{wv} - a)} \frac{d\gamma_{lr}}{dT_s}. \end{aligned} \tag{49}$$

One important difference between the continuum and the other feedbacks is that the continuum is transparent across all wavenumbers at low surface temperatures, and only becomes optically

thick at high surface temperatures. We approximate the continuum's emissivity as $1 - e^{-\tau_{cnt}}$, which correctly captures the limiting behavior of an emitter at small and large optical thickness ($\tau_{cnt} \ll 1$ versus $\tau_{cnt} \gg 1$). The continuum can only dominate the atmosphere's emission at wavenumbers at which CO_2 and H_2O absorption are weak, so we set the effective width of the continuum equal to the width of the window region $\Delta \tilde{\nu}_{surf}$, defined above. The continuum feedback is then

$$
\begin{aligned}
-\lambda_{cnt} &= \int_{cnt} \pi \frac{dB_\nu}{dT}\Big|_{T_{cnt}} \frac{dT_{cnt}}{dT_s} d\nu \\
&\approx c_{cnt} \times \pi \frac{dB_{\tilde{\nu}}}{dT}\Big|_{T_{cnt}} \times \frac{dT_{cnt}}{dT_s} \times \Delta \tilde{\nu}_{surf}(1 - e^{-\tau_{cnt}})
\end{aligned}
\tag{50}
$$

where c_{cnt} is again a scaling constant. The sign of λ_{cnt} is positive because the bulk lapse rate decreases with warming, $d\gamma_{lr}/dT_s < 0$. As discussed above, this means the H_2O continuum acts as a positive/destabilizing feedback and has the opposite sign of the negative/stabilizing H_2O band feedback.

e. CO_2 band feedback
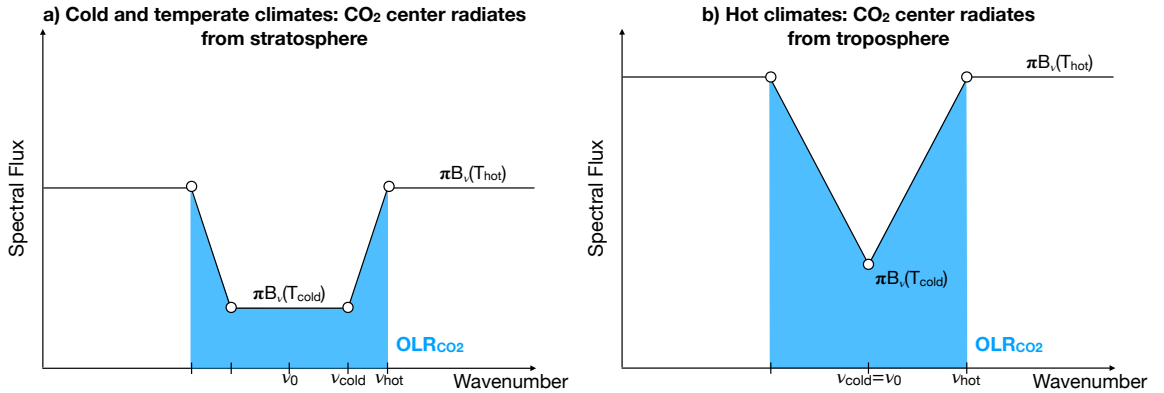
FIG. 6. A CO_2 "ditch" model: the CO_2 band emits $\pi B_\nu(T_{cold})$ in its center, its flanks emit $\pi B_\nu(T_{hot})$, and the slopes in-between are approximated as linear and symmetric. Shaded blue area is the OLR contribution from the CO_2 band. Left: In cold climates or at high CO_2 abundances the CO_2 band center radiates from the stratosphere. Right: In hot climates or at low CO_2 abundances the CO_2 band center radiates from the troposphere.

Next, we consider the CO_2 feedback. Unlike the H_2O band and continuum, however, the emission temperature of CO_2 varies strongly with wavenumber, which makes it difficult to approximate the

35

$_{701}$ CO$_2$ feedback integral via simple multiplication. Instead we introduce an idealized CO$_2$ "ditch"

$_{702}$ model, illustrated in Figure 6. Our approach is closely related to the CO$_2$ forcing models of

$_{703}$ Wilson and Gea-Banacloche (2012) and Jeevanjee et al. (2021b) – in Appendix A we show that

$_{704}$ our ditch model can also be used to rederive the results of those previous studies, underlining the

$_{705}$ close relationship between forcing and feedbacks.

$_{706}$ We approximate the CO$_2$ band as symmetric around the central frequency $\nu_0 = 667$ cm^{-1}. The

$_{707}$ center of the band emits $\pi B_\nu(T_{\text{cold}})$ while outside the band the emission is $\pi B_\nu(T_{\text{hot}})$. Here T_{cold}

$_{708}$ and T_{hot} are cold and hot emission temperatures, while ν_{hot} and ν_{cold} denote the edges of the CO$_2$

$_{709}$ ditch. At low and moderate surface temperatures the CO$_2$ band center around 667 cm^{-1} radiates

$_{710}$ from the stratosphere, so T_{cold} is equal to the stratospheric temperature. However, this situation

$_{711}$ is no longer true at high surface temperatures. Physically, the tropopause rises as the surface

$_{712}$ warms, so if one warms the surface while holding CO$_2$ concentration fixed (this is implicit in the

$_{713}$ definition of a climate feedback), parts of the CO$_2$ band that were previously in the stratosphere

$_{714}$ have to start radiating from the troposphere. Eventually, even the CO$_2$ band center radiates from

$_{715}$ the troposphere so the rectangular CO$_2$ ditch turns into a triangular trough (see Fig. 6b). Here we

$_{716}$ leave our expressions general to allow for either situation.

$_{717}$ The CO$_2$ band is relatively narrow, so we can neglect the wavenumber-dependence of the Planck

$_{718}$ function and evaluate it at the center of the CO$_2$ band, $\pi B_\nu(T) \approx \pi B_{\nu_0}(T)$. Treating the slopes of

$_{719}$ the CO$_2$ ditch as piecewise-linear, the OLR from the CO$_2$ band is then simply the blue area under

$_{720}$ the ditch in Figure 6a,

$$
\begin{aligned}
\text{OLR}_{\text{co}_2} &= 2\int_{\nu_0}^{\nu_{\text{hot}}} \pi B_{\nu_0}(T_{\text{co}_2})d\nu \\
&= \left[\pi B_{\nu_0}(T_{\text{hot}}) + \pi B_{\nu_0}(T_{\text{cold}})\right](\nu_{\text{hot}} - \nu_{\text{cold}}) + 2\pi B_{\nu_0}(T_{\text{cold}})(\nu_{\text{cold}} - \nu_0).
\end{aligned}
\tag{51}
$$

$_{721}$ The OLR change in response to some climate perturbation is

$$
\begin{aligned}
\Delta\text{OLR}_{\text{co}_2} &= \text{OLR}'_{\text{co}_2} - \text{OLR}_{\text{co}_2} \\
&= \left[\pi B_{\nu_0}(T'_{\text{hot}}) + \pi B_{\nu_0}(T'_{\text{cold}})\right](\nu'_{\text{hot}} - \nu'_{\text{cold}}) - \left[\pi B_{\nu_0}(T_{\text{hot}}) + \pi B_{\nu_0}(T_{\text{cold}})\right](\nu_{\text{hot}} - \nu_{\text{cold}}) + \\
&\quad 2\pi B_{\nu_0}(T'_{\text{cold}})(\nu'_{\text{cold}} - \nu_0) - 2\pi B_{\nu_0}(T_{\text{cold}})(\nu_{\text{cold}} - \nu_0),
\end{aligned}
\tag{52}
$$

722 where primes indicate perturbed variables. For the CO_2 band feedback the relevant perturbation is
723 a change in surface temperature ΔT_s, while for the forcing the relevant perturbation is a change in
724 q_{co_2} (see Appendix A). If ΔT_s is small enough we can series expand and drop higher-order terms.
725 For example, the perturbation of the emission at the CO_2 band edge is

$$\pi B_{\nu_0}(T'_{\text{hot}}) = \pi B_{\nu_0}(T_{\text{hot}}) + \pi \frac{dB_{\nu_0}}{dT}\Big|_{T_{\text{hot}}} \frac{dT_{\text{hot}}}{dT_s}\Delta T_s,$$

726 with similar expressions for T'_{cold}, ν'_{cold}, and ν'_{cold}. Plugging back into Equation 52, the feedback of
727 the CO_2 ditch is

$$
\begin{aligned}
-\lambda_{\text{co}_2} &= \lim_{\Delta T_s \to 0} \frac{\Delta \text{OLR}_{\text{co}2}}{\Delta T_s} \\
&= \left[\pi \frac{dB_{\nu_0}}{dT}\bigg|_{T_{\text{hot}}} \frac{dT_{\text{hot}}}{dT_s} + \pi \frac{dB_{\nu_0}}{dT}\bigg|_{T_{\text{cold}}} \frac{dT_{\text{cold}}}{dT_s} \right] (\nu_{\text{hot}} - \nu_{\text{cold}}) \\
&\quad + \left[\pi B_{\nu_0}(T_{\text{hot}}) + \pi B_{\nu_0}(T_{\text{cold}}) \right] \left(\frac{d\nu_{\text{hot}}}{dT_s} - \frac{d\nu_{\text{cold}}}{dT_s} \right) \\
&\quad + 2\pi \frac{dB_{\nu_0}}{dT}\bigg|_{T_{\text{cold}}} \frac{dT_{\text{cold}}}{dT_s} (\nu_{\text{cold}} - \nu_0) + 2 B_{\nu_0}(T_{\text{cold}}) \frac{d\nu_{\text{cold}}}{dT_s}.
\end{aligned}
\tag{53}
$$

728 Equation 53 gives the most general expression for the feedback of the CO_2 ditch. Geometrically,
729 the blue area under the CO_2 ditch changes if the flanks and center rise while the edges remain fixed
730 (terms proportional to dT_{hot}/dT_s and dT_{cold}/dT_s), or if the edges move while the flanks and center
731 of the ditch remain fixed (terms proportional to $d\nu_{\text{hot}}/dT_s$ and $d\nu_{\text{cold}}/dT_s$). To evaluate Equation
732 53 we thus need to specify how the parameters T_{hot}, T_{cold}, ν_{hot} and ν_{cold} vary as a function of
733 surface temperature.

734   At cold surface temperatures we again ignore H_2O absorption around the CO_2 band so $T_{\text{hot}} = T_s$.
735 Similarly, the tropopause is low and the CO_2 band center radiates from the stratosphere, so
736 $T_{\text{cold}} = T_{\text{strat}}$ and $dT_{\text{cold}}/dT_s = 0$. As in Section 5a, we find the band edges ν_{hot} and ν_{cold} by
737 solving $T_{\text{co}_2}(\nu_{\text{hot}}) = T_s$ and $T_{\text{co}_2}(\nu_{\text{cold}}) = T_{\text{strat}}$. The results are $\nu_{\text{hot}} = \nu_0 + l_\nu \log[\tau^*_{\text{co}_2}(\nu_0) q_{\text{co}_2}]$, and
738 $\nu_{\text{cold}} = \nu_0 + l_\nu \log[\tau^*_{\text{co}_2}(\nu_0) q_{\text{co}_2}(T_{\text{strat}}/T_s)^{2/\gamma_{\text{lr}}}]$. We can see that the hot CO_2 band edge does not
739 change under surface warming, $d\nu_{\text{hot}}/dT_s = 0$, while the sensitivity of the cold or stratospheric

37

band edge to surface warming is

$$
\begin{aligned}
\frac{d\nu_{\text{cold}}}{dT_s} &= \left.\frac{\partial \nu_{\text{cold}}}{\partial T_s}\right|_{\gamma_{\text{lr}}} + \left.\frac{\partial \nu_{\text{cold}}}{\partial \gamma_{\text{lr}}}\right|_{T_s} \frac{d\gamma_{\text{lr}}}{dT_s} \\
&= -\frac{2l_\nu}{\gamma_{\text{lr}} T_s} + \frac{2l_\nu}{\gamma_{\text{lr}}^2} \log\left(\frac{T_s}{T_{\text{strat}}}\right) \frac{d\gamma_{\text{lr}}}{dT_s}.
\end{aligned}
\tag{54}
$$

The lapse rate change $d\gamma_{\text{lr}}/dT_s$ is always negative, so the portion of the CO_2 band inside the stratosphere shrinks, $d\nu_{\text{cold}}/dT_s < 0$. Geometrically, since ν_{hot} stays fixed while ν_{cold} moves towards the center of the CO_2 band, the CO_2 band slope becomes shallower and the blue area under the CO_2 ditch increases – an OLR increase, or a stabilizing feedback. Physically, this is a simple consequence of a rising tropopause. As the surface warms, the tropopause moves to lower pressures, thus moving more of CO_2's emission from the cold stratosphere into the warmer tropopause. Plugging back into Equation 53, the CO_2 band feedback at cold surface temperatures is

$$
\begin{aligned}
-\lambda_{\text{co}_2}^{cool} = \left.\pi\frac{dB_{\nu_0}}{dT}\right|_{T_s} \frac{2}{\gamma_{\text{lr}}} \log\left(\frac{T_s}{T_{\text{strat}}}\right) + &\left[\pi B_{\nu_0}(T_s) - \pi B_{\nu_0}(T_{\text{strat}})\right] \\
&\times \left(\frac{2l_\nu}{\gamma_{\text{lr}} T_s} - \frac{2l_\nu}{\gamma_{\text{lr}}^2} \log\left(\frac{T_s}{T_{\text{strat}}}\right) \frac{d\gamma_{\text{lr}}}{dT_s}\right)
\end{aligned}
\tag{55}
$$

At high surface temperatures the CO_2 band center moves into the tropopause and the rectangular ditch turns into a triangle (see lower left in Fig. 4, and sketch in Fig. 6b). We set $\nu_{\text{cold}} = \nu_0$, where the central wavenumber ν_0 is set by the spectroscopic properties of CO_2 and so is fixed under surface warming ($d\nu_{\text{cold}}/dT_s = 0$). The emission temperature in the center of the CO_2 band is now $T_{\text{cold}} = T_{\text{co}_2}(\nu_0)$, where T_{co_2} is the emission temperature of CO_2 (Eqn. 26a). The crucial difference between high and low surface temperatures is that once the CO_2 band center moves into the tropopause T_{cold} is no longer constant,

$$
\begin{aligned}
\frac{dT_{\text{co}_2}(\nu_0)}{dT_s} &= \left.\frac{\partial T_{\text{co}_2}(\nu_0)}{\partial T_s}\right|_{\gamma_{\text{lr}}} + \left.\frac{\partial T_{\text{co}_2}(\nu_0)}{\partial \gamma_{\text{lr}}}\right|_{T_s} \frac{d\gamma_{\text{lr}}}{dT_s} \\
&= \frac{T_{\text{co}_2}(\nu_0)}{T_s} - \frac{T_{\text{co}_2}(\nu_0)}{2} \log[q_{\text{co}_2}\tau_{\text{co}_2}^*(\nu_0)] \frac{d\gamma_{\text{lr}}}{dT_s}.
\end{aligned}
\tag{56}
$$

38

The outer edges of the CO_2 band at high temperatures are set by water vapor absorption, $T_{hot} = \min[T_{H_2O}(\nu_0), T_{cnt}]$. We treat H_2O as Simpsonian, so $dT_{hot}/dT_s \approx 0$, and also ignore non-Simpsonian shifts in the outer CO_2 band edge, $d\nu_{hot}/dT_s \approx 0$. Plugging back into Equation 53, the feedback at high surface temperatures is then

$$
\begin{aligned}
-\lambda_{co_2}^{hot} &= \pi \left.\frac{dB_{\nu_0}}{dT}\right|_{T_{cold}} \frac{dT_{cold}}{dT_s}(\nu_{hot} - \nu_{cold}) \\
&= \pi \left.\frac{dB_{\nu_0}}{dT}\right|_{T_{cold}} \frac{dT_{cold}}{dT_s} l_\nu \log\left[\tau_{co_2}^*(\nu_0) q_{co_2} \left(\frac{T_{hot}}{T_s}\right)^{\frac{2}{\gamma_{lr}}}\right].
\end{aligned}
\tag{57}
$$

Geometrically, the behavior of the CO_2 band at high temperatures is dictated by the rise in the center of the band, dT_{cold}/dT_s. Since the band center emits more in response to surface warming, $dT_{cold}/dT_s > 0$, the blue area under the triangular ditch goes up – again, an OLR increase, which leads to a stabilizing feedback. Physically, once the center of the CO_2 band radiates from inside the troposphere, we have $dT_{cold}/dT_s \propto -d\gamma_{lr}/dT_s$, which means the rate at which emission increases is highly sensitive to the rate at which the upper atmosphere warms via the changing lapse rate.

Finally, when does the CO_2 band center change from a stratospheric radiator at low T_s to a tropospheric radiator at high T_s, which also determines the transition between $\lambda_{co_2}^{cool}$ and $\lambda_{co_2}^{hot}$? Based on line-by-line calculations with 400 ppm of CO_2, Appendix B shows that the smoothed emission temperature in the CO_2 band center moves out of the stratosphere at surface temperatures above 310 K. We therefore identify 310 K as the transition point between the low-temperature and high-temperature CO_2 feedback regimes. Note, however, that this value also depends on CO_2 concentration.

Multiplying the low-temperature regime with a scaling constant c_{co_2}, similar to our other spectral feedbacks, the overall CO_2 band feedback is thus

$$
\lambda_{co_2} = \begin{cases} c_{co_2} \times \lambda_{co_2}^{cool} & \text{if } T_s \le 310 \text{ K} \\ \lambda_{co_2}^{hot} + b & \text{if } T_s > 310 \text{ K.} \end{cases}
\tag{58}
$$

where we choose the constant b to ensure that λ_{co_2} remains continuous at 310 K (in practice b is always of order unity, $b \sim 0.5$).
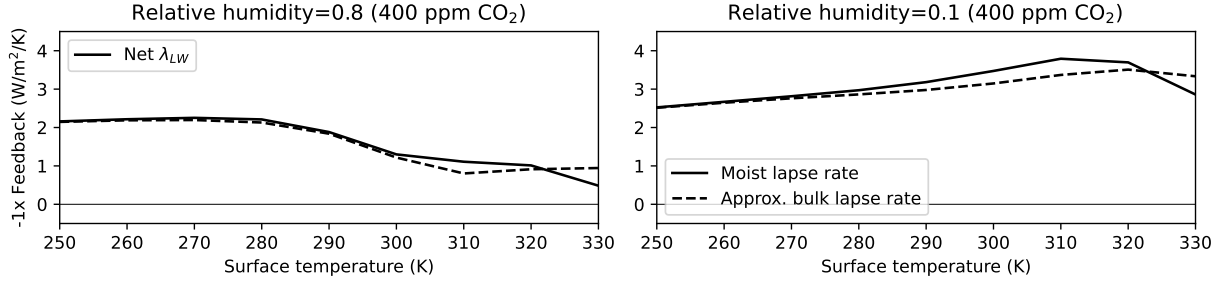
FIG. 7. The impact of the bulk lapse rate approximation on longwave feedbacks is modest below ~320 K, but becomes significant at high temperatures. Solid lines are numerical feedbacks calculated assuming the atmosphere follows a moist adiabatic profile, dashed lines are numerical feedbacks calculated assuming the atmosphere follows our bulk lapse rate approximation.

f. Validation against LBL calculations

To test our analytic feedback expressions we again use 1D calculations with PyRADS. One potential issue is that our derivations use the bulk lapse rate approximation, and so might differ from realistic feedbacks. Figure 7 compares feedbacks calculated with a moist adiabat to feedbacks with bulk lapse rate profiles. Overall, the bulk lapse rate approximation only introduces minor errors in λ_{LW} over the temperature range $250 - 320$ K. We therefore consider the bulk lapse rate approximation sufficiently accurate below 320 K, while care should be taken when applying our analytic expressions to extremely hot climates. To better match the derivations, the PyRADS calculations here also use vertical profiles with a bulk lapse rate, so $T = T_s (p/p_s)^{\gamma_{lr}}$. We explore the surface temperature-dependence of spectral feedbacks at high and low relative humidity (RH=0.8 and RH=0.1), without CO_2 and with 400 ppm of CO_2, for four sets of calculations in total.

To compare our analytic expressions against the 1D calculations we need to specify the scaling constants c_{surf}, c_{H_2O}, c_{cnt}, and c_{co_2}. We pick these constants to match the 1D calculations at RH=0.8 and 400 ppm of CO_2. The temperature-dependence varies significantly between different feedbacks, so we choose c_{surf} to match λ_{surf} at low temperatures ($T_s = 250$ K), c_{cnt} to match λ_{cnt} at high temperatures ($T_s = 330$ K), and c_{H_2O} and c_{co_2} to match λ_{H_2O} and λ_{co_2} around Earth's present-day mean temperature ($T_s = 290$ K). Table 1 gives the resulting values for the above 1D calculations with bulk lapse rates, and for another set of 1D calculations with moist lapse rates. In agreement with Figure 7, the scaling constants vary little between the two sets of calculations.

40

₈₀₀ In this Section we choose the scaling constants to match the idealized 1D calculations with bulk
₈₀₁ lapse rates, while Section 6 considers a feedback calculation specifically for present-day Earth, and
₈₀₂ so uses the scaling constants that match the moist adiabatic calculations. Regardless of the exact
₈₀₃ values, the scaling constants are always of order unity.
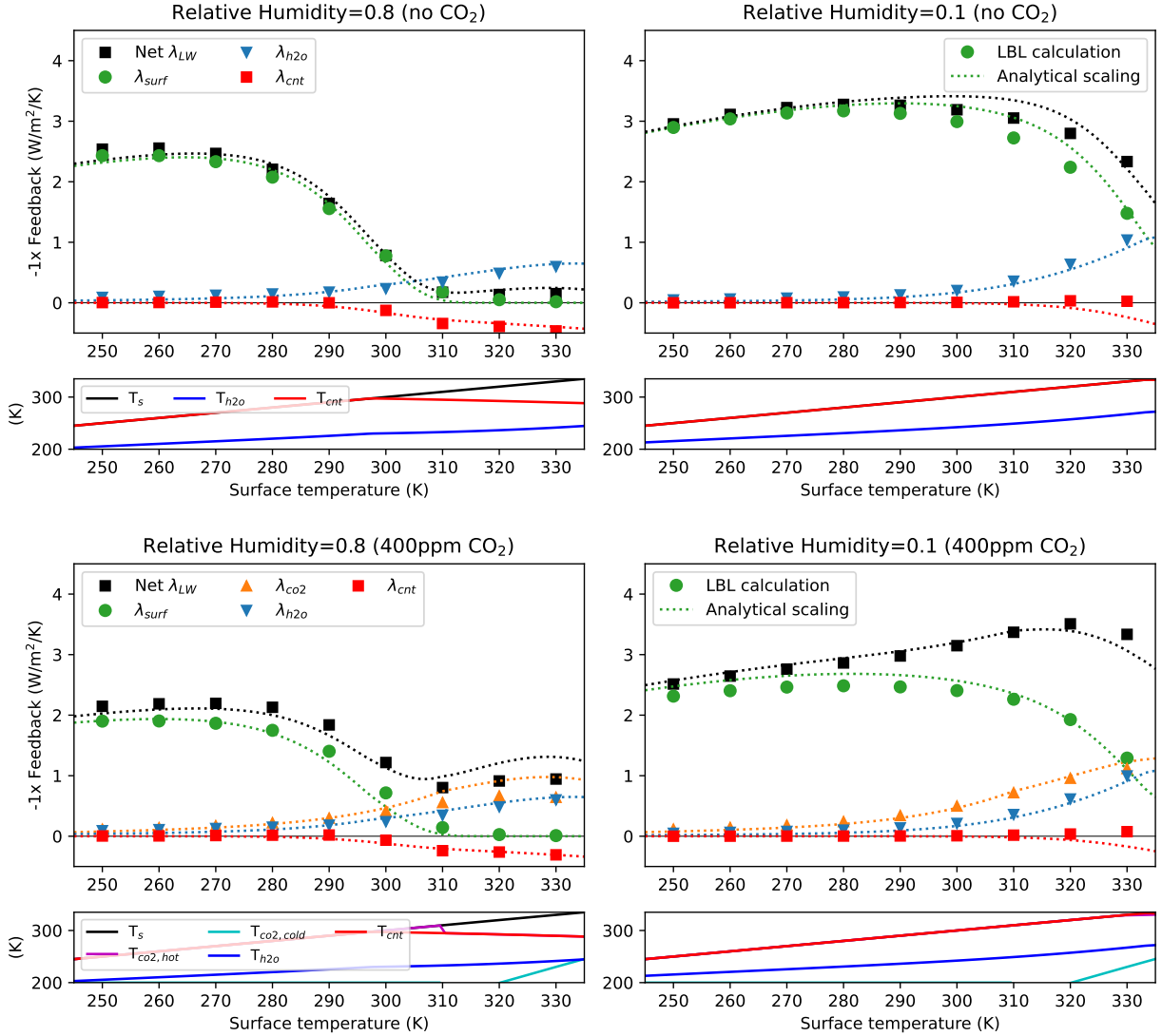
₈₀₄ Fɪɢ. 8. Spectral feedbacks calculated using PyRADS and assuming a bulk lapse rate (symbols), compared
₈₀₅ against the analytic scalings (lines). Top row shows calculations without CO_2, bottom row with 400ppm of CO_2.
₈₀₆ The large panels show feedbacks while small panels show the corresponding analytic emission temperatures.

₈₀₇ Figure 8 shows that our analytic expressions successfully capture the basic state-dependence of
₈₀₈ λ_{LW} as well as of its spectral constituents. The longwave feedback λ_{LW} is sensitive to changes in

41

surface temperature, but it also varies in response to humidity and CO_2 changes. Comparing the left and right columns in Figure 8, λ_{LW} becomes larger with decreasing relative humidity (also see McKim et al. 2021). Comparing the top and bottom rows, adding CO_2 to an atmosphere without any CO_2 evens out the temperature-dependence of λ_{LW}, by decreasing λ_{LW} at cold temperatures and increasing λ_{LW} at high temperatures. Importantly, the analytic expressions capture most of the variation in λ_{LW}, including its state-dependence.

To understand the behavior of λ_{LW} we turn to the individual spectral feedbacks. The surface feedback λ_{surf} is generally the dominant term in the spectral decomposition. Without CO_2, λ_{surf} makes up at least 90% of λ_{LW} below 300 K. The presence of CO_2 decreases λ_{surf} but even in this case λ_{surf} makes up at least 60% of λ_{LW} below 300 K. Our analytic expressions thus agree with previous studies which showed that Earth's longwave feedback is dominated by the surface feedback (Koll and Cronin 2018; Raghuraman et al. 2019). This situation changes at high temperatures, however, once the surface window closes, at which point λ_{LW} becomes dominated by atmospheric feedbacks.

In line with Section 4, the CO_2 band feedback acts to stabilize Earth's climate in warm climates, and its importance increases with surface temperature. Below 300 K, λ_{co_2} contributes less than 20% of the total feedback, but its magnitude grows rapidly with surface temperature such that at 330 K and high relative humidity λ_{co_2} makes up almost 70% of λ_{LW}. Interestingly, for large RH λ_{co_2} becomes equal to λ_{surf} at surface temperatures around ~ 305 K. Extrapolating from these 1D calculations to Earth's spatial feedback pattern, we can expect that Earth's feedback is dominated by the surface in most regions, but that atmospheric feedbacks become important in the inner tropics – an issue explored in detail in Section 6.

Finally, again in line with our analytic results, the two water vapor feedbacks λ_{H_2O} and λ_{cnt} have opposing signs. At high relative humidity λ_{H_2O} and λ_{cnt} partially cancel. In contrast, at low relative humidity λ_{cnt} becomes negligible while λ_{H_2O} only changes moderately – a non-Simpsonian effect. The different sensitivity to RH arises because the continuum's optical thickness scales as $\tau_{\text{cnt}} \propto \text{RH}^2$, whereas the optical thickness in the water vapor bands only scales as $\tau_{H_2O} \propto \text{RH}$. Decreases in relative humidity therefore increase λ_{LW} both by increasing the surface feedback λ_{surf} and by reducing λ_{cnt}, so that H_2O acts as a net stabilizing feedback. Comparing λ_{H_2O} and λ_{co_2} at present-day CO_2 levels, we see that the two feedbacks are roughly equal in magnitude. Non-

TABLE 2. Summary of main theoretical results.

Emission temperatures

$$T_{co_2}(\nu) = T_s \left(\frac{1}{\tau_{co_2}^*(\nu) q_{co_2}} \right)^{\gamma_{lr}/2}$$

$$T_{H_2O}(\nu) = T_0 \left(\frac{1+\gamma_{wv}\gamma_{lr}}{\tau_{H_2O}^*(\nu)RH} \right)^{\frac{\gamma_{lr}}{1+\gamma_{wv}\gamma lr}} \left(\frac{T_s}{T_0} \right)^{\frac{1}{1+\gamma_{wv}\gamma lr}}$$

$$T_{cnt} = T_0 \left(\frac{(2\gamma_{wv}-a)\gamma_{lr}}{\tau_{cnt}^* RH^2} \right)^{\frac{1}{2\gamma_{wv}-a}}$$

Feedbacks

$$-\lambda_{surf} = c_{surf} \times \pi \frac{dB_{\check{\nu}}}{dT} \Big|_{T_s} \Delta\tilde{\nu}_{surf} e^{-\tau_{cnt}}$$

$$-\lambda_{H_2O} = c_{H_2O} \times \pi \frac{dB_{\check{\nu}}}{dT} \Big|_{T_{H_2O}(\tilde{\nu})} \times \frac{dT_{H_2O}(\nu)}{dT_s} \times \Delta\nu_{H_2O}$$

$$-\lambda_{cnt} = c_{cnt} \times \pi \frac{dB_\gamma}{dT} \Big|_{\tilde{\nu},T_{cnt}} \times \frac{dT_{cnt}}{dT_s} \times \Delta\tilde{\nu}_{surf} (1-e^{-\tau_{cnt}})$$

$$-\lambda_{co_2} = \begin{cases} c_{co_2} \times \frac{2\pi}{\gamma_{lr}} \frac{dB_{\nu_0}}{dT} \Big|_{T_s} \log\left(\frac{T_s}{T_{strat}} \right) - \left[\pi B_{\nu_0}(T_s) - \pi B_{\nu_0}(T_{strat}) \right] \times \frac{d\nu_{cold}}{dT_s} & \text{at low } T_s \\ \pi \frac{dB_{\nu_0}}{dT} \Big|_{T_{cold}} \frac{dT_{cold}}{dT_s} (\nu_{hot} - \nu_{cold}) + b & \text{at high } T_s \end{cases}$$

Simpsonian H_2O effects are thus about as important as the CO_2 band for Earth's current longwave feedback.

6. The Spatial Pattern of λ_{LW}

In the previous two sections we demonstrated that the analytic expressions summarized in Table 2 accurately capture the behavior of Earth's emission temperature T_{rad} as well as the state-dependence of λ_{LW}. These feedback expressions can interpreted as either a model for the global-mean feedback or as a model for the local feedback of an isolated atmospheric column, so the state-dependence of λ_{LW} shown in Figure 8 should also appear as a spatial-dependence in Earth's clear-sky longwave feedback.

In this section we therefore analyze the spatial pattern of λ_{LW} for Earth's present-day climate. First, we generate a map of λ_{LW} using the radiative kernel technique (Soden et al. 2008). Next, we generate a map of λ_{LW} using our analytic expressions. The radiative kernel technique cannot be used to determine the feedback contributions of individual gases and our analytic expressions only account for the feedback from Earth's dominant greenhouse gases, H_2O and CO_2, whereas the radiative kernel includes additional greenhouse gases such as O_3 and CH_4. We therefore

split λ_{LW} into only two terms, namely the surface feedback λ_{surf} and the atmospheric feedback $\lambda_{atm} = \lambda_{LW} - \lambda_{surf}$. Despite the idealizations in our analytic approach compared to a full radiative kernel, we find that the resulting feedback maps are in qualitative agreement. This allows us to attribute the spatial pattern of λ_{LW}, as deduced from the radiative kernel, to geographic variations in the inputs of our analytic model.

a. Inputs for feedback maps

For the kernel calculation we use the HadGEM2 radiative kernel. For consistency with the analytic model (which assumes the stratosphere is isothermal and at a fixed temperature), we set the kernel to zero in the stratosphere. The tropopause is defined as in Soden et al. (2008): the tropopause pressure p_{tp} increases linearly with latitude, from 0.1 bar at the equator to 0.3 bar at the poles. The analytic model also assumes RH stays fixed under surface warming, so we do not include RH changes in the kernel calculation. Doing so is justified because the RH feedback only makes a minor contribution to λ_{LW} in individual climate models, and it moreover tends to cancel in the multi-model mean (Zelinka et al. 2020). To compute the forced response we use HadGEM2 climatologies from the CMIP5 archive for a preindustrial control simulation and an abrupt-4xCO2 simulation, where the climatologies are 50-year averages (for 4xCO$_2$, years 100-150 after increasing CO$_2$). Multiplying the kernel with the forced response gives a map of the change in top-of-atmosphere (TOA) radiation (Soden et al. 2008). To compute a feedback one additionally needs to normalize the change in TOA radiation by a change in surface temperature. Consistent with our assumption of an isolated atmospheric column we compute local-local feedback maps, that is, we divide the local change in OLR deduced from the kernel by the local change in surface temperature (Feldl and Roe 2013; Armour et al. 2013; Bloch-Johnson et al. 2020). To distinguish between surface and atmospheric feedbacks in the kernel method we compute the clear-sky longwave feedback λ_{LW} and the surface feedback λ_{surf}, where the second is equal to the surface kernel; the atmospheric feedback is then computed as the residual $\lambda_{atm} = \lambda_{LW} - \lambda_{\text{surf}}$.

We compare the kernel-derived feedback maps against maps from our analytic expressions. The surface feedback λ_{surf} is the same as in Section 5, while the atmospheric feedback is the sum over all atmospheric terms $\lambda_{atm} = \lambda_{\text{co}_2} + \lambda_{\text{H}_2\text{O}} + \lambda_{\text{cnt}}$. The analytic expressions require six input parameters: CO$_2$ concentration, surface temperature T_s, stratosphere temperature T_{strat}, relative humidity RH,

44

temperature lapse rate γ_{lr}, and the change in lapse rate under surface warming $d\gamma_{lr}/dT_s$. Except for the lapse rate change $d\gamma_{lr}/dT_s$, all these inputs can be obtained from a single climate state (here, the HadGEM2 preindustrial state) and do not require knowledge of the climate's forced response. CO_2 is set to be spatially uniform at 400 ppm (results are highly similar if using a preindustrial 285 ppm); the surface temperature T_s is taken as the air temperature at 2m; and the stratospheric temperature T_{strat} is set equal to the temperature at the tropopause pressure level, $T_{strat} = T(p_{tp})$, where p_{tp} is defined using via the above tropopause definition of Soden et al. (2008). The relative humidity RH is set equal to the column relative humidity, defined as the ratio between the atmospheric column's water vapor path and its water vapor path at saturation (e.g., Bretherton et al. 2005),

$$\text{RH} = \frac{\text{WVP}}{\text{WVP}^*}, \tag{59}$$

$$= \frac{\int_{p_{tp}}^{p_s} q \, dp/g}{\int_{p_{tp}}^{p_s} q^* \, dp/g}. \tag{60}$$

Here the vertical integral is taken from the tropopause p_{tp} down to the surface to exclude the strongly sub-saturated stratosphere. One could in principle also approximate RH using other measures of atmospheric humidity; however, the column relative humidity is a natural choice because it correctly captures the atmosphere's total water vapor path, which in turn determines the width of the window region and λ_{surf}.

Next, the lapse rate $\gamma_{lr} = d\ln T/d\ln p$ varies strongly in the vertical. We compute a bulk lapse rate using a mass-weighted vertical average,

$$\gamma_{lr} = \frac{1}{p_1 - p_{tp}} \int_{p_{tp}}^{p_1} \frac{p}{T} \frac{dT}{dp} dp, \tag{61}$$

where the average is taken from the tropopause p_{tp} down to a near-surface pressure p_1. Some polar regions have such strong surface inversions that the inferred bulk lapse rate becomes negative, whereas our derivations break down if $\gamma_{lr} < 0$. At the same time, the map of γ_{lr} should reflect near-surface inversions over subtropical eastern ocean basins and deep boundary layers over tropical land, discussed below. We therefore define p_1 similar to p_{tp}, as varying linearly in latitude from $p_1 = 1$ bar at the equator to $p_1 = 0.85$ bar at the poles. One could also evaluate γ_{lr} using the bulk lapse rate definition from Equation 6 in combination with a tropopause definition; however,

45

this approach makes the inferred lapse rates quite sensitive to the tropopause definition, which we side-step by using the mass-weighted average in Equation 61 instead. Finally, the only input in our analytic expressions that requires information about the climate's forced response is the change in lapse rate $d\gamma_{\mathrm{lr}}/dT_s$, which is computed using the difference in γ_{lr} between the HadGEM2 4xCO$_2$ and preindustrial simulations.
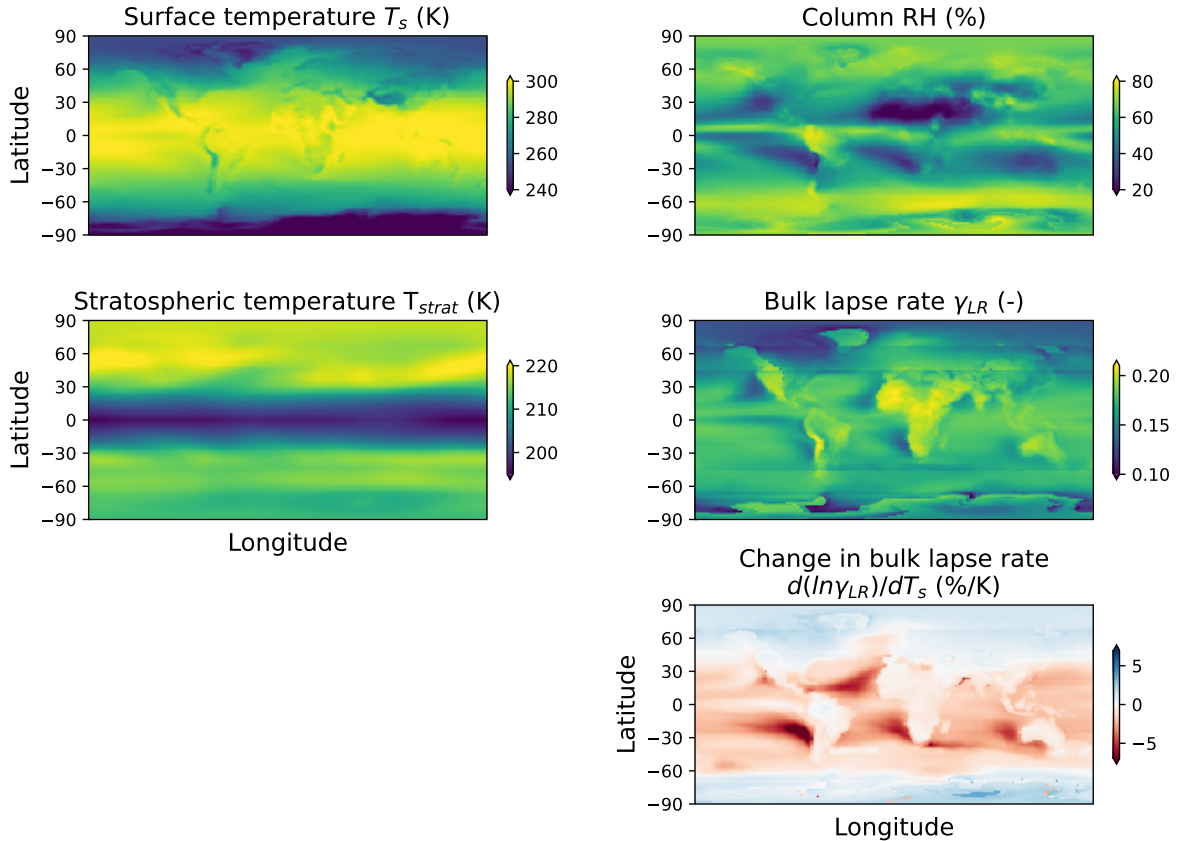
FIG. 9. Input data used to evaluate the analytic feedback maps in Figure 10. The top four panels show fields from a HadGEM2 preindustrial simulation. The bottom right panel shows the normalized bulk lapse rate change $d\ln(\gamma_{\mathrm{lr}})/dT_s$ computed using the HadGEM2 4xCO$_2$ and preindustrial simulations.

Figure 9 shows maps of the input data from HadGEM2, which we use below to evaluate the analytic expressions. In the top two rows, large variations are notable in the maps of surface temperature T_s, column relative humidity RH, and bulk lapse rate γ_{lr}. In contrast, apart from minor stationary wave patterns in the northern mid-latitudes, the stratospheric temperature T_{strat} is zonally fairly uniform and varies by only about 20 K between the equator and poles. The bottom row

46

shows the normalized bulk lapse change, $d\ln(\gamma_{\mathrm{lr}})/dT_s = 1/(\Delta\gamma_{\mathrm{lr}}) \times (\Delta\gamma_{\mathrm{lr}}/\Delta T_s)$, computed using the bulk lapse rate difference $\Delta\gamma_{\mathrm{lr}}$ between 4xCO2 and preindustrial simulations. The bulk lapse rate change shows an equator-pole contrast, with a decrease in γ_{lr} at low and mid latitudes and an increase in γ_{lr} at high latitudes. This contrast is in line with previous studies – for a moist adiabat the atmospheric temperature-pressure profile becomes less steep under warming, so γ_{lr} decreases in the tropics, while the opposite occurs at high latitudes (e.g., Payne et al. 2015; Cronin and Jansen 2016; Stuecker et al. 2018). There is also a noticeable tropical land-ocean contrast in the bulk lapse-rate change, with tropical land areas showing near-zero lapse-rate change. This is likely due to compensation between moist-adiabatic warming aloft, which is uniform across the tropics and tends to decrease γ_{lr}, and amplified land surface warming, which increases γ_{lr} (Byrne and O'Gorman 2013). Conversely, subtropical eastern ocean basins have the same moist adiabatic warming aloft but *suppressed* surface warming, both of which contribute to strong decreases in γ_{lr}.

b. *Feedback maps*

Figure 10 shows the feedback maps resulting from kernel and analytic calculations. Overall, we find good qualitative agreement between kernel-derived feedbacks and our analytic approximations. The global pattern of λ_{LW} in both maps shows clear contrasts between the high latitudes, subtropics, and inner tropics (Fig. 10, top row). λ_{LW} is smallest in the inner tropics, especially in the intertropical convergence zone (ITCZ), while it is largest in the subtropics, especially over eastern ocean basins. The agreement is less good at small scales, with the analytic map of λ_{LW} showing less regional structure and deviating from the kernel-derived map in continental interiors and over the Southern Ocean. This is plausible given the idealizations in our derivations, such as representing realistic vertical temperature profiles by a smooth power-law. However, small-scale differences tend to cancel when taking a zonal or global mean. The zonal-mean of λ_{LW} in our analytic estimate agrees with the zonal-mean of the kernel λ_{LW} to within 11% at each latitude. The global-mean values of λ_{LW} are almost identical, with -2.15 W/m^2/K for the kernel calculation and -2.16 W/m^2/K for the analytic estimate. Note that these global mean averages are weighted by the HadGEM2 pattern of surface warming, which is required to convert a local-local feedback map into a global mean (Feldl and Roe 2013; Armour et al. 2013).

47
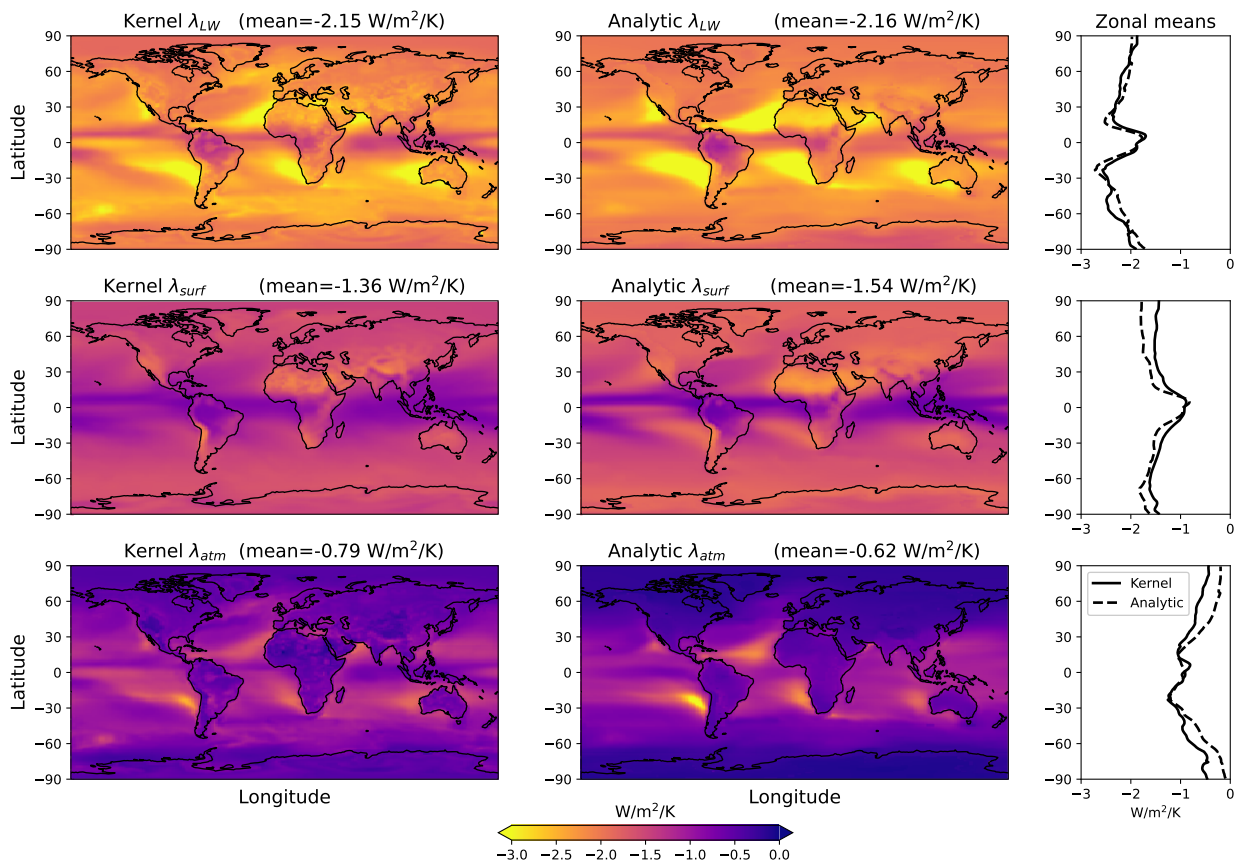
FIG. 10. Feedback maps showing feedbacks computed with a radiative kernel (left column), or with our analytic expressions (middle column). The analytic maps are calculated from the inputs shown in Figure 9. Top row shows the net longwave clear-sky feedback λ_{LW}, middle row the surface component λ_{surf}, and bottom row and the atmospheric component λ_{atm}. Means above each subpanel are area-weighted global means that are weighted by the pattern of surface warming.

The qualitative agreement between the λ_{LW} maps also holds separately for surface and atmo-spheric feedbacks, though differences are larger here. The kernel-derived map of λ_{surf} is almost uniform at high latitudes, large in magnitude over subtropical desert regions, and small in magnitude over the ITCZ. The analytic map of λ_{surf} qualitatively matches this pattern, though it overpredicts the magnitude of λ_{surf} in the global mean by 0.18 W/m^2/K, or 13%. Conversely, the analytic esti-mate underpredicts λ_{atm} relative to the kernel-derived map in the global mean by 0.17 W/m^2/K, or 22%. In addition, the analytic λ_{atm} map predicts that the atmospheric feedback goes almost to zero at the poles, whereas the kernel-derived λ_{atm} map shows a small but clearly non-zero feedback. The strong differences at the poles again presumably arise because our derivations fail to capture the

48

Surface fraction of total LW feedback, $\lambda_{surf}/\lambda_{LW}$
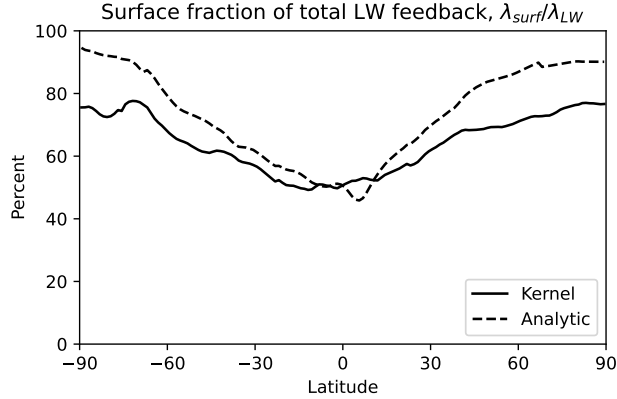
FIG. 11. Zonal mean fraction of the surface feedback to the net feedback, $\lambda_{\mathrm{surf}}/\lambda_{LW}$, based on the radiative kernel (solid) and our analytic expressions (dashed).

atmospheric feedback response in areas with inversions and other complex temperature-pressure profiles.

In addition to an overall spatial agreement, both kernel and analytic feedback calculations agree that the surface dominates the net longwave feedback. Figure 11 shows that the surface's contribution to the total feedback is about 50% at low latitudes and increases towards the poles, reaching about 75% in the kernel maps and over 90% in the analytic maps. One plausible reason why the analytic maps tend to overestimate $\lambda_{\mathrm{surf}}/\lambda_{LW}$ at high latitudes is that our expressions do not include minor greenhouse gases such as ozone or methane. Any additional atmospheric absorption from such gases reduces the window width via $\Delta\nu_{\mathrm{surf}} \times e^{-\tau_{\mathrm{cnt}}}$ and thus also the surface feedback λ_{surf} (also see Feng et al. 2022). This effect should be most clearly visible at high latitudes, where water vapor concentrations are low and $\Delta\nu_{\mathrm{surf}}$ is large, while at low latitudes $\Delta\nu_{\mathrm{surf}} \times e^{-\tau_{\mathrm{cnt}}}$ is already small due to the water vapor continuum, leaving less room for other greenhouse gases to affect λ_{surf}. Nevertheless, in line with the results from Section 5, both kernel and analytic maps show that λ_{LW} is dominated by λ_{surf} across most of the globe. In contrast, atmospheric feedbacks only start to rival λ_{surf} in the inner tropics and particularly inside the ITCZ (Fig. 10). Our finding agrees with other published estimates: the simple area-weighted global mean of $\lambda_{\mathrm{surf}}/\lambda_{LW}$ is 60% in our kernel calculation and 67% in our analytic estimate, well in line with the results of Raghuraman et al. (2019) who deduced 63% using a different methodology. Similarly, Feng et al. (2022) found that $\lambda_{\mathrm{surf}}/\lambda_{LW}$ varies between 88% at the poles to 50% in the tropics, in good agreement with

49

Figure 11. We conclude that our analytic model of λ_{LW} has notable biases at regional scales but it is sufficient to understand the factors that underlie the large-scale pattern of λ_{LW}, which we turn to next.

c. *What controls the large-scale pattern of λ_{LW}?*
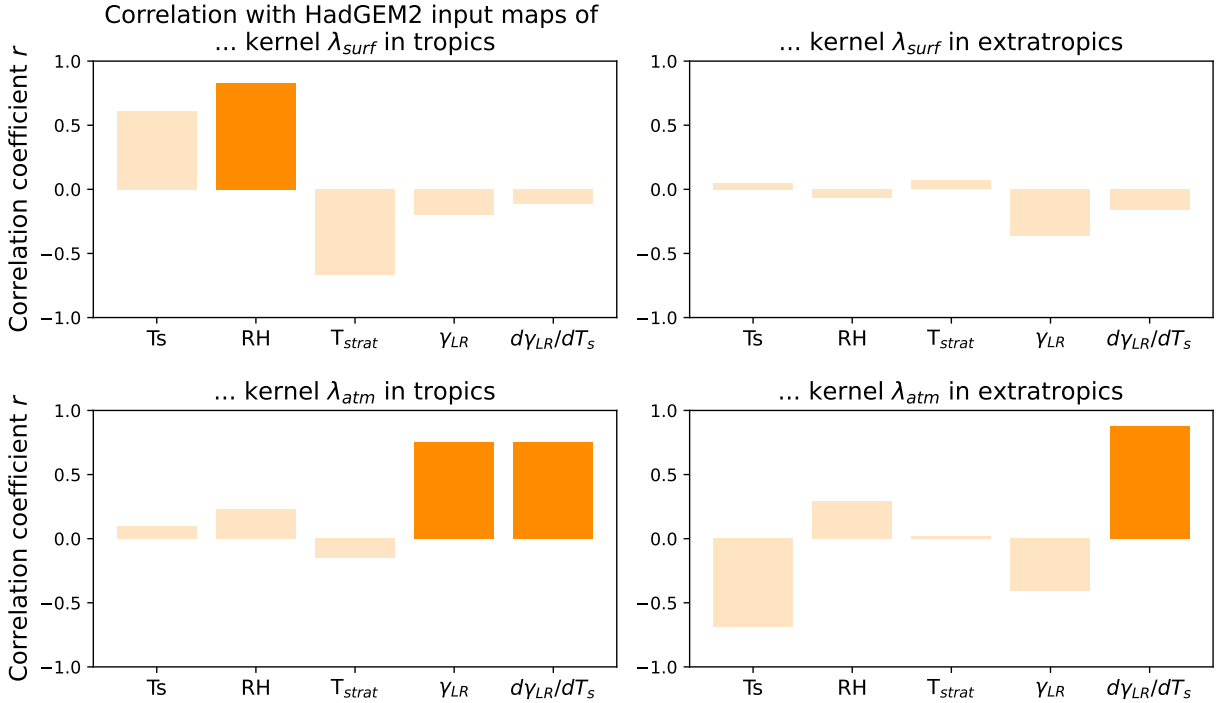
FIG. 12. Spatial correlation between the kernel-derived feedback maps of λ_{surf} and λ_{atm} (Figure 10, left column), and the inputs to our analytic model (Figure 9). Top row shows correlations between inputs and λ_{surf}, bottom row shows correlations between inputs and λ_{atm}. Left column shows correlations inside the tropics, right column shows correlations in the extratropics. Dark colors highlight particularly strong correlations ($|r| \geq 0.75$), while the tropics/extratropics are defined as all points equatorward/poleward of 30° latitude.

The match between our analytic model and the kernel calculation implies that one can explain much of the spatial structure of λ_{LW} in terms of the analytic model's input parameters. We do this by calculating correlations between λ_{surf} and λ_{atm} from the kernel-derived feedback maps against the analytic model's five main inputs: surface temperature T_s, column relative humidity RH, stratospheric temperature T_{strat}, bulk lapse rate γ_{lr}, and the change in bulk lapse rate under

50

warming $d\gamma_{\mathrm{lr}}/dT_s$. Spatial CO_2 contrasts are small (e.g., Fraser et al. 1983), and so do not need to be considered here.

Figure 12 shows the resulting spatial correlations between the kernel-derived feedback maps (left column of Figure 10) and the five inputs from HadGEM2 (Figure 9). Because the feedback maps differ strongly between tropics and extratropics in terms of zonal variation and magnitude, we compute correlations separately in these two regions (data are split based on being equatorward or poleward of 30° latitude). Based on the inherent correlations between the five input maps, we consider a correlation significant if its coefficient exceeds $|r| \geq 0.75$ (the largest intra-input correlations are $r = -0.71$ between T_s and T_{strat} in the tropics, and $r = -0.76$ between T_s and $d\gamma_{\mathrm{lr}}/dT_s$ in the extratropics; not shown).

In line with our analytic model, we find that the kernel-derived λ_{surf} is strongly correlated with column RH in the tropics ($r = 0.83$), while it does not show strong correlation with any inputs in the extratropics ($|r| < 0.4$). This underlines the importance of the subtropical dry radiator fin regions for λ_{surf}, which are clearly visible as the dark blue regions in Figure 9 (top right) and the yellow regions in Figure 10 (center left). As expected, the sign of the correlation is positive which means λ_{surf} becomes less negative, or less stabilizing, as column RH increases.

Next, we find λ_{atm} is most strongly correlated with γ_{lr} and $d\gamma_{\mathrm{lr}}/dT_s$ in the tropics ($r = 0.75$ for both), and with $d\gamma_{\mathrm{lr}}/dT_s$ in the extratropics ($r = 0.88$). Of the two parameters that show strong correlations with λ_{atm} in the tropics, γ_{lr} and $d\gamma_{\mathrm{lr}}/dT_s$, which one is more important? We performed a test with the analytical model in which we set $d\gamma_{\mathrm{lr}}/dT_s = 0$ (not shown). Doing so eliminates most tropical structure in the map of λ_{atm}, which indicates that λ_{atm} is largely determined by $d\gamma_{\mathrm{lr}}/dT_s$, not γ_{lr}. The correlation between λ_{atm} and $d\gamma_{\mathrm{lr}}/dT_s$ is positive, which is intuitive: λ_{atm} becomes more negative if the upper atmosphere warms more relative to the surface, i.e. if γ_{lr} decreases. The spatial variability of λ_{atm} is largest in the tropics, and can be can be understood in terms of the map of $d\gamma_{\mathrm{lr}}/dT_s$ already discussed in Section 6a: tropical λ_{atm} is large over subtropical eastern ocean basins due to suppressed surface warming, and small over land due to enhanced surface warming, where these warming patterns are relative to the approximately uniform warming of the tropical free troposphere (Byrne and O'Gorman 2013).

The correlations shown in Figure 12 are between fields derived from two independent methods, and so are non-trivial. Appendix C shows that the same analysis performed with λ_{surf} and λ_{atm}

from our analytic feedback maps identifies the same dominant relations (e.g., λ_{surf} is most strongly correlated with column RH in the tropics), though most correlation coefficients are unsurprisingly even larger (e.g., $r = 0.93$ for the analytic λ_{surf} and tropical column RH). Our results thus underline that the spatial pattern of λ_{LW} can be understood, at least in rough terms and on large spatial scales, by Earth's spatial pattern of relative humidity and lapse rate changes. Relative humidity and lapse rate changes dominate the pattern of λ_{LW} in the tropics, where they control λ_{surf} and λ_{atm} respectively, while lapse rate changes dominate the pattern of λ_{atm} in the extratropics.

7. Discussion & Conclusions

In this paper we have presented a novel decomposition of Earth's clear-sky longwave feedback λ_{LW} into four spectral components, namely a surface Planck feedback (λ_{surf}) and three atmospheric feedbacks: a CO_2 band feedback (λ_{co_2}), a (non-Simpsonian) water vapor band feedback (λ_{H_2O}), and a destabilizing water vapor continuum feedback (λ_{cnt}). We have derived simple analytic expressions for each of these spectral feedbacks, which accurately reproduce the results of line-by-line calculations and qualitatively match the feedback map computed from a radiative kernel. In principle one could extend this approach even further to account for additional complicating factors, such as the effect of additional greenhouse gases or a more realistic stratosphere. However, our results already show that from a radiative perspective the factors determining λ_{LW} can be understood fairly easily, adding further support to the close agreement between observations and climate models.

The picture of Earth's clear-sky longwave feedback that emerges from this perspective is relatively simple, consisting of a surface feedback plus atmospheric feedbacks from CO_2 and H_2O. At present the surface feedback λ_{surf} is the most important contributor in the global-mean and at most latitudes, with its spatial pattern determined by the distribution of atmospheric water vapor. λ_{surf} is largest in the dry subtropics, consistent with the view that these are the locus of Earth's stabilizing longwave feedback (Pierrehumbert 1995; McKim et al. 2021), and smallest in the inner tropics, where the surface's emission is blocked by the H_2O continuum. The atmospheric feedbacks from the CO_2 and H_2O bands play a supporting role to λ_{surf} at mid and high latitudes, but they rival the surface feedback in the inner tropics, with the global pattern of λ_{atm} largely determined by the pattern of the atmospheric lapse rate change $d\gamma_{\mathrm{lr}}/dT_s$. The H_2O continuum provides a negligible feedback

52

below ~ 310 K (see Section 5), but the continuum itself is still important through its influence on λ_{surf}.

This spectral picture is arguably a more intuitive starting point for reasoning about different climates than the conventional decomposition of λ_{LW} into Planck, Lapse Rate and Water Vapor feedbacks. As discussed by Cronin and Dutta (in revision at QJRMS), it is non-trivial to accurately estimate the supposedly-simple Planck feedback from first principles. Similarly, one can qualitatively reason that Lapse Rate and Water Vapor feedbacks both increase in magnitude under global warming, but these are large and of opposite sign, so it is difficult to predict their net change and, by extension, the T_s-dependence of λ_{LW}, in the conventional decomposition without resorting to numerical models. The strong cancellations between Planck, Lapse Rate and Water Vapor feedbacks can be alleviated by considering conventional feedbacks in a fixed relative humidity framework (Ingram 2010; Held and Shell 2012), but this comes at the cost that the state-dependence of the Planck feedback is no longer trivial to understand at fixed RH.

In contrast, the state-dependence of λ_{LW} is fairly straightforward to understand from a spectral perspective, at least in broad brushstrokes. For present-day Earth the T_s-dependence of λ_{LW} is dominated by the surface in most regions. If relative humidity is fixed, λ_{surf} increases at very cold temperatures, peaks around $260 - 290$ K depending on RH, and then decreases again (see Section 5). The decrease is rapid at high RH due to the H_2O continuum, but much slower at low RH. Atmospheric feedbacks also have state-dependence. All of them increase in magnitude as the atmosphere warms, and are further amplified by a weakening lapse rate. In the tropics the state-dependence of λ_{LW} is thus set by the interplay between a decreasing surface feedback and increasing atmospheric feedbacks. This can lead to surprising dynamics – at high RH, λ_{surf} decreases in magnitude more rapidly with warming than the atmospheric feedbacks from $\lambda_{\mathrm{co_2}}$ and λ_{H_2O} increase. As a result λ_{LW} becomes non-monotonic with warming and develops a local minimum around ~ 310 K, which leads to a local maximum in climate sensitivity (Seeley and Jeevanjee 2021).

The state-dependence of λ_{LW} at temperatures far above ~ 310 K is beyond the scope of this paper, but a spectral perspective points to the importance of stabilizing H_2O and CO_2 bands versus the destabilizing H_2O continuum as Earth approaches the runaway greenhouse. The main caveat here is that Earth's net feedback does not necessarily stay dominated by λ_{LW} at very high surface

temperatures, and atmospheric feedbacks are also complicated at high temperatures by effects such as non-dilute thermodynamics and surface pressure changes (Goldblatt et al. 2013; Ramirez et al. 2014).

There are several remaining shortcomings in our analysis of λ_{LW} that are beyond the scope of this paper. A major one is our assumption that the atmosphere can be described by a single bulk lapse rate, such that temperature has to monotonically decrease with altitude. In the real world inversions are common, particularly in polar regions and over subtropical oceans. Comparable to the long-standing discussion about how to interpret the Lapse Rate feedback at high latitudes in the conventional decomposition (e.g., Cai and Lu 2009; Payne et al. 2015; Stuecker et al. 2018; Boeke et al. 2021; Henry et al. 2021), we therefore expect that our approach here only provides a first step towards understanding the processes which shape λ_{LW} in inversion regions.

Another assumption is that we ignore stratospheric changes, even though stratospheric cooling induced by rising CO_2 levels is a major and robust signal of anthropogenic warming (e.g., Vallis et al. 2014). It is notable that the radiative changes due to stratospheric cooling are also hard to intuitively explain using conventional feedbacks. Climate model analyses typically treat the stratosphere's fast radiative adjustment to CO_2 changes as distinct from Planck, Lapse Rate, and Water Vapor feedbacks. Our derivations here sidestep this issue and treat T_{strat} as a fixed parameter. Similarly, our derivations ignore the potential feedback from relative humidity changes. In reality there is no guarantee that relative humidity will remain constant under global warming, let alone would have been similar in past climates. In principle our analysis starting from the emission level approximation can be extended to estimate the feedbacks associated with changes in either RH or T_{strat}; RH changes would lead to a feedback term proportional to $\partial T_{\text{rad}}/\partial \text{RH}$, while stratospheric changes would lead to a feedback term proportional to $\partial T_{\text{rad}}/\partial T_{\text{strat}}$.

Data availability statement. HadGEM2 GCM data is publicly available in CMIP data archives. The HadGEM2 radiative kernel is available at `https://archive.researchdata.leeds.ac.uk/382`. Scripts to compute analytic feedbacks will be posted online once the manuscript is accepted for publication.
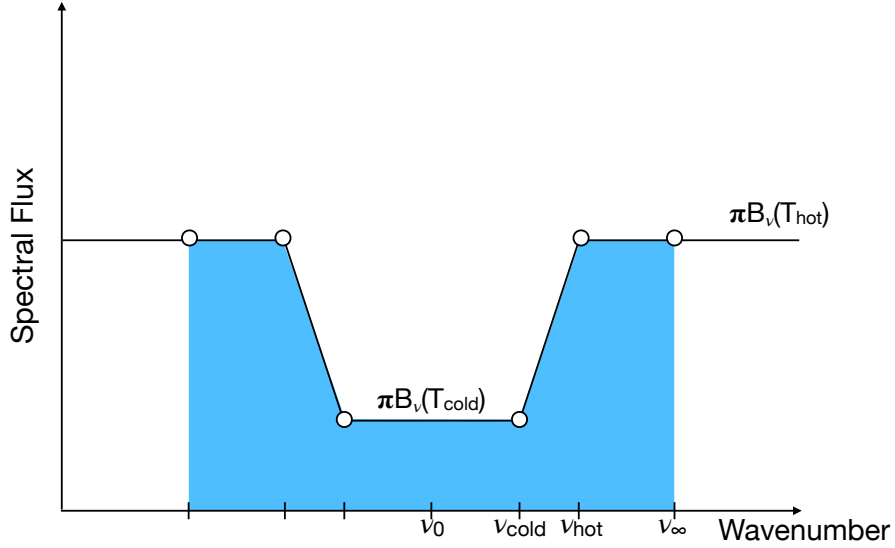
CO$_2$ Forcing

FIG. A1. CO$_2$ ditch model for the CO$_2$ forcing. The shaded blue area is the OLR contribution from the CO$_2$ band as well as neighboring spectral regions. The band edges ν_{hot} and ν_{cold} vary in response to CO$_2$ concentration q_{co_2}, while ν_∞ is sufficiently far away from the CO$_2$ band to be constant with respect to q_{co_2}.

The CO$_2$ ditch model can be used to explain the CO$_2$ forcing in addition to the CO$_2$ band feedback. This section rederives the CO$_2$ forcing expressions from Wilson and Gea-Banacloche (2012) and Jeevanjee et al. (2021b), which are valid as long as the CO$_2$ band center radiates from the stratosphere. Note that our CO$_2$ band feedback model only considers OLR changes inside the CO$_2$ band (see Figure 6). This is because the effect of CO$_2$ on $\lambda_{\mathrm{H_2O}}$ or λ_{surf} is separately considered in the derivation of those feedbacks. Forcing is defined as the OLR change integrated across all wavenumbers, however, so here we need to consider the expanded shaded region shown in Figure A1. The OLR integrated across this expanded region, OLR$_+$, is

$$
\begin{aligned}
\mathrm{OLR}_+ &= 2 \int_{\nu_0}^{\nu_{\nu_\infty}} \pi B_{\nu_0}(T_{\mathrm{rad}}) d\nu \\
&= \left[\pi B_{\nu_0}(T_{\mathrm{hot}}) + \pi B_{\nu_0}(T_{\mathrm{cold}}) \right] (\nu_{\mathrm{hot}} - \nu_{\mathrm{cold}}) + 2\pi B_{\nu_0}(T_{\mathrm{cold}})(\nu_{\mathrm{cold}} - \nu_0) + \\
&\quad 2\pi B_{\nu_0}(T_{\mathrm{hot}})(\nu_\infty - \nu_{\mathrm{hot}}).
\end{aligned}
\tag{A1}
$$

The foricng from a doubling of CO_2 is then

$$
\begin{aligned}
F_{co_2}^{2x} &= -\frac{d\text{OLR}_+}{d\log_2(q_{co_2})} \\
&= -\ln(2)\frac{d\text{OLR}_+}{d\ln q_{co_2}} \\
&= -\ln(2)\left(\left[\pi B_{\nu_0}(T_{\text{hot}}) + \pi B_{\nu_0}(T_{\text{cold}})\right]\left(\frac{d\nu_{\text{hot}}}{d\ln q_{co_2}} - \frac{d\nu_{\text{cold}}}{d\ln q_{co_2}}\right) + 2\pi B_{\nu_0}(T_{\text{cold}})\frac{d\nu_{\text{cold}}}{d\ln q_{co_2}} - \right. \\
&\quad \left. 2\pi B_{\nu_0}(T_{\text{hot}})\frac{d\nu_{\text{hot}}}{d\ln q_{co_2}}\right)
\end{aligned}
\tag{A2}
$$

The minus sign in the first line ensures that forcing is positive when OLR decreases, while the base-2 logarithm is necessary because forcing is defined with respect to a CO_2 doubling. In the second step we then change the logarithm's base to the natural logarithm, while in the third step we treat the emission temperatures T_{hot} and T_{cold} as constant. This is valid because the derivative of OLR with respect to q_{co_2} is taken at fixed T_s (i.e., at fixed surface temperature, the temperature outside the CO_2 band and in the stratosphere are both independent of CO_2 concentration).

The CO_2 band edges are defined by $T_{co_2}(\nu_{\text{hot}}) = T_{hot}$ and $T_{co_2}(\text{cold}) = T_{\text{strat}}$. Solving for ν_{hot} and ν_{cold} we find

$$
\nu_{\text{hot}} = \nu_0 + l_\nu \log\left[q_{co_2}\tau_{co_2}^*(\nu_0)\left(\frac{T_{\text{hot}}}{T_s}\right)^{2/\gamma_{\text{lr}}}\right]
\tag{A3}
$$

$$
\nu_{\text{cold}} = \nu_0 + l_\nu \log\left[q_{co_2}\tau_{co_2}^*(\nu_0)\left(\frac{T_{\text{strat}}}{T_s}\right)^{2/\gamma_{\text{lr}}}\right].
\tag{A4}
$$

We can see that the CO_2 band edges shift equally in response to a CO_2 increase:

$$
\frac{d\nu_{\text{hot}}}{d\ln q_{co_2}} = \frac{d\nu_{\text{cold}}}{d\ln q_{co_2}} = l_\nu.
\tag{A5}
$$

It follows that the first term proportional to $d\nu_{\text{hot}}/d\ln q_{co_2} - d\nu_{\text{cold}}/d\ln q_{co_2}$ in Equation A2 is zero. The CO_2 forcing is thus

$$
F_{co_2}^{2x} = 2\ln(2)l_\nu\left(\pi B_{\nu_0}(T_{\text{hot}}) - \pi B_{\nu_0}(T_{\text{cold}})\right),
\tag{A6}
$$

which is identical to the analytic CO_2 forcing model in Jeevanjee et al. (2021b) (their Equations 7 and 14).

APPENDIX B

Transition from stratospheric to tropospheric CO_2 radiator fin
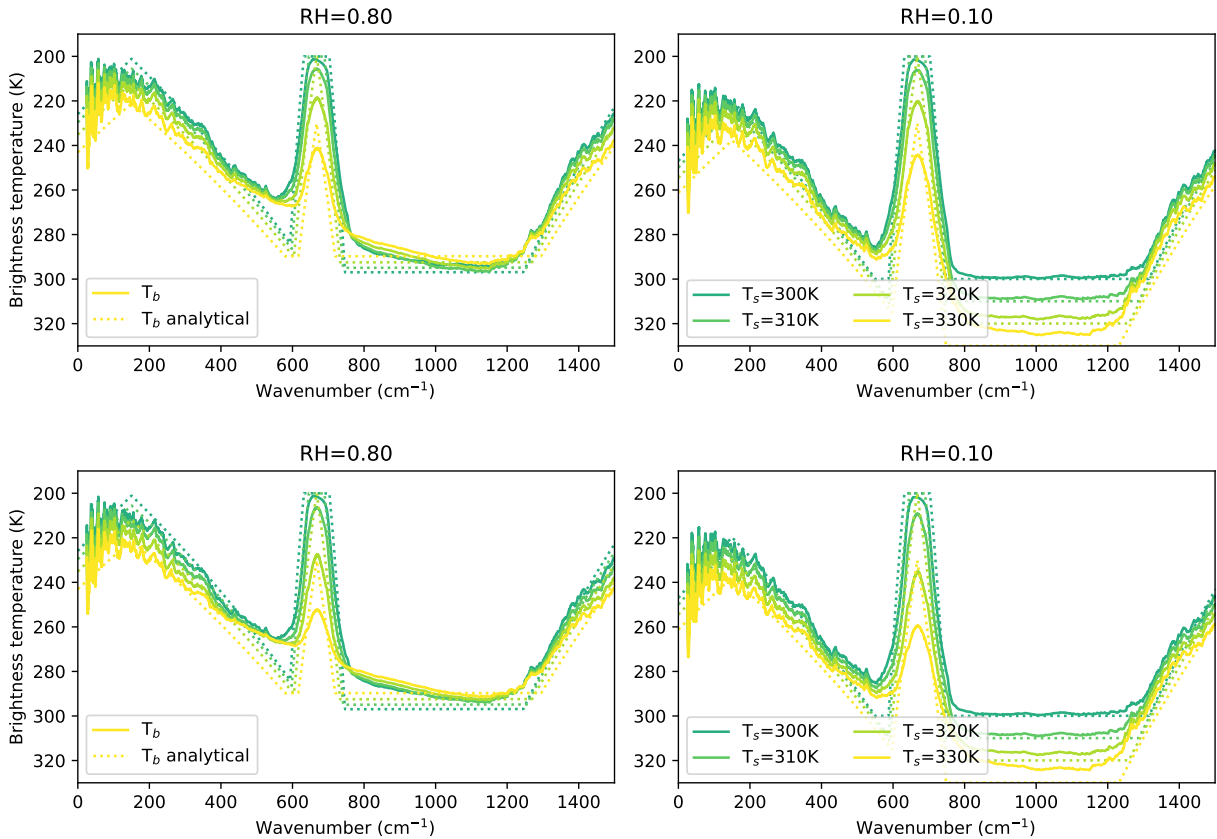
FIG. B1. Brightness temperatures computed from line-by-line calculations and smoothed with a 50 cm^{-1} median filter (solid), versus analytic emission temperatures (dashed). Top row: calculations use a bulk lapse-rate profile, $T(p) = T_s (p/p_s)^{\gamma_{lr}}$. Bottom row: calculations use a moist adiabat.

At high surface temperatures the CO_2 band center transitions from mainly radiating from the stratosphere to mainly radiating from the troposphere. Figure B1 shows smoothed brightness temperatures T_b computed from the 1D line-by-line calculations described in Section 5, with a CO_2 volume-mixing ratio of 400 ppm. In the middle of the CO_2 band, at about 667 cm^{-1}, CO_2 radiates from the troposphere at surface temperatures above ~ 310 K. In rough agreement with

57

the line-by-line results, our analytic CO_2 brightness temperatures predict this transition happens at a surface temperature of ~ 320 K (dashed lines in Fig. B1). In practice we therefore use a transition temperature of $T_{s,0} = 310$ K for 400 ppm of CO_2 to determine when CO_2 changes from a stratospheric to a tropospheric radiator.

APPENDIX C

Spatial correlations in analytic feedback maps
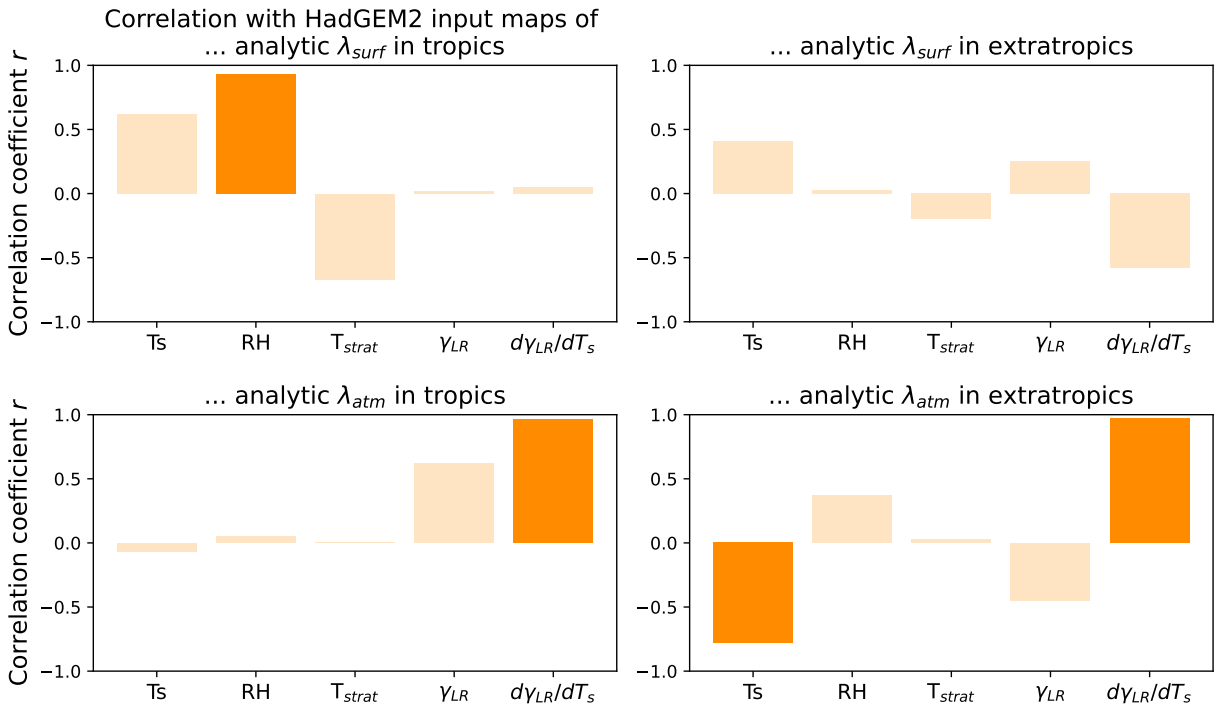
FIG. C1. Spatial correlation between the analytic feedback maps of λ_{surf} and λ_{atm} (Figure 10, right column), and the inputs to our analytic model (Figure 9). Top row shows correlations between inputs and λ_{surf}, bottom row shows correlations between inputs and λ_{atm}. Left column shows correlations inside the tropics, right column shows correlations in the extratropics. Dark colors highlight particularly strong correlations ($|r| \geq 0.8$).

Figure C1 repeats the same analysis as in Figure 12, but using the analytic feedback maps of λ_{surf} and λ_{atm}. Given that the analytic model is computed using the input fields from Figure 9, it is not surprising that most correlations between inputs and feedback maps are even higher than in Fig. 12. With the exception of λ_{atm} in the tropics, for which the correlation between the analytic

58

λ_{atm} and γ_{lr} is slightly lower than between kernel-derived λ_{atm} and γ_{lr}, Figure C1 identifies the same strong correlations as Figure 12.

References

Andrews, T., J. M. Gregory, and M. J. Webb, 2015: The Dependence of Radiative Forcing and Feedback on Evolving Patterns of Surface Temperature Change in Climate Models. *Journal of Climate*, **28 (4)**, 1630–1648, https://doi.org/10.1175/JCLI-D-14-00545.1.

Andrews, T., J. M. Gregory, M. J. Webb, and K. E. Taylor, 2012: Forcing, feedbacks and climate sensitivity in CMIP5 coupled atmosphere-ocean climate models. *Geophysical Research Letters*, **39 (9)**, https://doi.org/10.1029/2012GL051607.

Andrews, T., and Coauthors, 2018: Accounting for Changing Temperature Patterns Increases Historical Estimates of Climate Sensitivity. *Geophysical Research Letters*, **45 (16)**, 8490–8499, https://doi.org/10.1029/2018GL078887.

Armour, K. C., C. M. Bitz, and G. H. Roe, 2013: Time-Varying Climate Sensitivity from Regional Feedbacks. *Journal of Climate*, **26 (13)**, 4518–4534, https://doi.org/10.1175/JCLI-D-12-00544.1.

Bloch-Johnson, J., R. T. Pierrehumbert, and D. S. Abbot, 2015: Feedback temperature dependence determines the risk of high warming. *Geophysical Research Letters*, **42 (12)**, 2015GL064 240, https://doi.org/10.1002/2015GL064240.

Bloch-Johnson, J., M. Rugenstein, and D. S. Abbot, 2020: Spatial radiative feedbacks from internal variability using multiple regression. *Journal of Climate*, https://doi.org/10.1175/JCLI-D-19-0396.1.

Boeke, R. C., P. C. Taylor, and S. A. Sejas, 2021: On the Nature of the Arctic's Positive Lapse-Rate Feedback. *Geophysical Research Letters*, **48 (1)**, e2020GL091 109, https://doi.org/10.1029/2020GL091109.

Bretherton, C. S., P. N. Blossey, and M. Khairoutdinov, 2005: An Energy-Balance Analysis of Deep Convective Self-Aggregation above Uniform SST. *Journal of the Atmospheric Sciences*, **62 (12)**, 4273–4292, https://doi.org/10.1175/JAS3614.1.

Budyko, M. I., 1969: The effect of solar radiation variations on the climate of the Earth. *Tellus*, **21 (5)**, 611–619, https://doi.org/10.1111/j.2153-3490.1969.tb00466.x.

Byrne, M. P., and P. A. O'Gorman, 2013: Land–Ocean Warming Contrast over a Wide Range of Climates: Convective Quasi-Equilibrium Theory and Idealized Simulations. *Journal of Climate*, **26 (12)**, 4000–4016, https://doi.org/10.1175/JCLI-D-12-00262.1.

Cai, M., and J. Lu, 2009: A new framework for isolating individual feedback processes in coupled general circulation climate models. Part II: Method demonstrations and comparisons. *Climate Dynamics*, **32 (6)**, 887–900, https://doi.org/10.1007/s00382-008-0424-4.

Chung, E.-S., D. Yeomans, and B. J. Soden, 2010: An assessment of climate feedback processes using satellite observations of clear-sky OLR. *Geophysical Research Letters*, **37 (2)**, https://doi.org/10.1029/2009GL041889.

Crisp, D., S. B. Fels, and M. D. Schwarzkopf, 1986: Approximate methods for finding $CO2$ 15-Mm band transmission in planetary atmospheres. *Journal of Geophysical Research: Atmospheres*, **91 (D11)**, 11 851–11 866, https://doi.org/10.1029/JD091iD11p11851.

Cronin, T. W., and M. F. Jansen, 2016: Analytic radiative-advective equilibrium as a model for high-latitude climate. *Geophysical Research Letters*, **43 (1)**, 2015GL067 172, https://doi.org/10.1002/2015GL067172.

Ding, F., and R. T. Pierrehumbert, 2016: Convection in Condensible-rich Atmospheres. *The Astrophysical Journal*, **822 (1)**, 24, https://doi.org/10.3847/0004-637X/822/1/24.

Dufresne, J.-L., V. Eymet, C. Crevoisier, and J.-Y. Grandpeix, 2020: Greenhouse Effect: The Relative Contributions of Emission Height and Total Absorption. *Journal of Climate*, **33 (9)**, 3827–3844, https://doi.org/10.1175/JCLI-D-19-0193.1.

Elsasser, W. M., 1942: *Heat Transfer by Infrared Radiation in the Atmosphere*. Harvard university, Blue Hill meteorological observatory, Milton, Mass.

Feldl, N., and G. H. Roe, 2013: Four perspectives on climate feedbacks. *Geophysical Research Letters*, **40 (15)**, 4007–4011, https://doi.org/10.1002/grl.50711.

60

Feng, J., and Y. Huang, 2019: Diffusivity-Factor Approximation for Spectral Outgoing Longwave Radiation. *Journal of the Atmospheric Sciences*, **76 (7)**, 2171–2180, https://doi.org/10.1175/JAS-D-18-0246.1.

Feng, J., D. Paynter, and R. Menzel, 2022: How a stable greenhouse effect on Earth is maintained under global warming. Earth and Space Science Open Archive, https://doi.org/10.1002/essoar.10512049.1.

Fraser, P. J., G. I. Pearman, and P. Hyson, 1983: The global distribution of atmospheric carbon dioxide: 2. A review of provisional background observations, 1978–1980. *Journal of Geophysical Research: Oceans*, **88 (C6)**, 3591–3598, https://doi.org/10.1029/JC088iC06p03591.

Goldblatt, C., T. D. Robinson, K. J. Zahnle, and D. Crisp, 2013: Low simulated radiation limit for runaway greenhouse climates. *Nature Geoscience*, **6 (8)**, 661–667, https://doi.org/10.1038/ngeo1892.

Gordon, I. E., and Coauthors, 2017: The HITRAN2016 molecular spectroscopic database. *Journal of Quantitative Spectroscopy and Radiative Transfer*, **203**, 3–69, https://doi.org/10.1016/j.jqsrt.2017.06.038.

Hartmann, D. L., and K. Larson, 2002: An important constraint on tropical cloud - climate feedback. *Geophysical Research Letters*, **29 (20)**, 12–1–12–4, https://doi.org/10.1029/2002GL015835.

Held, I. M., and K. M. Shell, 2012: Using Relative Humidity as a State Variable in Climate Feedback Analysis. *Journal of Climate*, **25 (8)**, 2578–2582, https://doi.org/10.1175/JCLI-D-11-00721.1.

Henry, M., T. M. Merlis, N. J. Lutsko, and B. E. J. Rose, 2021: Decomposing the Drivers of Polar Amplification with a Single-Column Model. *Journal of Climate*, **34 (6)**, 2355–2365, https://doi.org/10.1175/JCLI-D-20-0178.1.

Huang, J., 2018: A Simple Accurate Formula for Calculating Saturation Vapor Pressure of Water and Ice. *Journal of Applied Meteorology and Climatology*, **57 (6)**, 1265–1272, https://doi.org/10.1175/JAMC-D-17-0334.1.

Huang, X., X. Chen, B. J. Soden, and X. Liu, 2014: The spectral dimension of longwave feedback in the CMIP3 and CMIP5 experiments. *Geophysical Research Letters*, **41 (22)**, 7830–7837, https://doi.org/10.1002/2014GL061938.

Huang, Y., and M. Bani Shahabadi, 2014: Why logarithmic? A note on the dependence of radiative forcing on gas concentration. *Journal of Geophysical Research: Atmospheres*, **119 (24)**, 2014JD022 466, https://doi.org/10.1002/2014JD022466.

Huang, Y., S. Leroy, P. J. Gero, J. Dykema, and J. Anderson, 2010: Separation of longwave climate feedbacks from spectral observations. *Journal of Geophysical Research: Atmospheres*, **115 (D7)**, https://doi.org/10.1029/2009JD012766.

Ingram, W., 2010: A very simple model for the water vapour feedback on climate change. *Quarterly Journal of the Royal Meteorological Society*, **136 (646)**, 30–40, https://doi.org/10.1002/qj.546.

Jeevanjee, N., and S. Fueglistaler, 2020: Simple Spectral Models for Atmospheric Radiative Cooling. *Journal of the Atmospheric Sciences*, **77 (2)**, 479–497, https://doi.org/10.1175/JAS-D-18-0347.1.

Jeevanjee, N., D. D. B. Koll, and N. Lutsko, 2021a: "Simpson's Law" and the Spectral Cancellation of Climate Feedbacks. *Geophysical Research Letters*, **48 (14)**, e2021GL093 699, https://doi.org/10.1029/2021GL093699.

Jeevanjee, N., J. T. Seeley, D. Paynter, and S. Fueglistaler, 2021b: An Analytical Model for Spatially Varying Clear-Sky CO2 Forcing. *Journal of Climate*, **34 (23)**, 9463–9480, https://doi.org/10.1175/JCLI-D-19-0756.1.

Kluft, L., S. Dacie, M. Brath, S. A. Buehler, and B. Stevens, 2021: Temperature-Dependence of the Clear-Sky Feedback in Radiative-Convective Equilibrium. *Geophysical Research Letters*, **48 (22)**, e2021GL094 649, https://doi.org/10.1029/2021GL094649.

Kluft, L., S. Dacie, S. A. Buehler, H. Schmidt, and B. Stevens, 2019: Re-Examining the First Climate Models: Climate Sensitivity of a Modern Radiative–Convective Equilibrium Model. *Journal of Climate*, **32 (23)**, 8111–8125, https://doi.org/10.1175/JCLI-D-18-0774.1.

Koll, D. D. B., and T. W. Cronin, 2018: Earth's outgoing longwave radiation linear due to H2O greenhouse effect. *Proceedings of the National Academy of Sciences*, **115 (41)**, 10 293–10 298, https://doi.org/10.1073/pnas.1809868115, https://www.pnas.org/content/115/41/10293.full.pdf.

Koll, D. D. B., and T. W. Cronin, 2019: Hot Hydrogen Climates Near the Inner Edge of the Habitable Zone. *The Astrophysical Journal*, **881 (2)**, 120, https://doi.org/10.3847/1538-4357/ab30c4, 1907.13169.

Li, J., 2000: Gaussian Quadrature and Its Application to Infrared Radiation. *Journal of the Atmospheric Sciences*, **57 (5)**, 753–765, https://doi.org/10.1175/1520-0469(2000)057<0753:GQAIAT>2.0.CO;2.

Manabe, S., and R. T. Wetherald, 1967: Thermal Equilibrium of the Atmosphere with a Given Distribution of Relative Humidity. *Journal of the Atmospheric Sciences*, **24**, 241–259, https://doi.org/10.1175/1520-0469(1967)024<0241:TEOTAW>2.0.CO;2.

McKim, B. A., N. Jeevanjee, and G. K. Vallis, 2021: Joint Dependence of Longwave Feedback on Surface Temperature and Relative Humidity. *Geophysical Research Letters*, **48 (18)**, e2021GL094 074, https://doi.org/10.1029/2021GL094074.

Meraner, K., T. Mauritsen, and A. Voigt, 2013: Robust increase in equilibrium climate sensitivity under global warming. *Geophysical Research Letters*, **40 (22)**, 5944–5948, https://doi.org/10.1002/2013GL058118.

Mlawer, E. J., V. H. Payne, J.-L. Moncet, J. S. Delamere, M. J. Alvarado, and D. C. Tobin, 2012: Development and recent evaluation of the MT_CKD model of continuum absorption. *Phil. Trans. R. Soc. A*, **370 (1968)**, 2520–2556, https://doi.org/10.1098/rsta.2011.0295.

Pan, F., and X. Huang, 2018: The Spectral Dimension of Modeled Relative Humidity Feedbacks in the CMIP5 Experiments. *Journal of Climate*, **31 (24)**, 10 021–10 038, https://doi.org/10.1175/JCLI-D-17-0491.1.

Payne, A. E., M. F. Jansen, and T. W. Cronin, 2015: Conceptual model analysis of the influence of temperature feedbacks on polar amplification. *Geophysical Research Letters*, **42 (21)**, 2015GL065 889, https://doi.org/10.1002/2015GL065889.

Pierrehumbert, R., 1995: Thermostats, radiator fins and the local runaway greenhouse. *Journal of the Atmospheric Sciences*, **52**, 1784–1806.

Pierrehumbert, R. T., 2010: *Principles of Planetary Climate*. Cambridge University Press, Cambridge, UK.

Raghuraman, S. P., D. Paynter, and V. Ramaswamy, 2019: Quantifying the Drivers of the Clear Sky Greenhouse Effect, 2000–2016. *Journal of Geophysical Research: Atmospheres*, **n/a (n/a)**, https://doi.org/10.1029/2019JD031017.

Ramirez, R. M., R. K. Kopparapu, V. Lindner, and J. F. Kasting, 2014: Can Increased Atmospheric CO2 Levels Trigger a Runaway Greenhouse? *Astrobiology*, **14 (8)**, 714–731, https://doi.org/10.1089/ast.2014.1153.

Romps, D. M., 2016: Clausius–Clapeyron Scaling of CAPE from Analytical Solutions to RCE. *Journal of the Atmospheric Sciences*, **73 (9)**, 3719–3737, https://doi.org/10.1175/JAS-D-15-0327.1.

Romps, D. M., J. T. Seeley, and J. P. Edman, 2022: Why the forcing from carbon dioxide scales as the logarithm of its concentration. *Journal of Climate*, **35 (13)**, 4027–4047, https://doi.org/10.1175/JCLI-D-21-0275.1.

Seeley, J. T., 2018: Convection, Radiation, and Climate: Fundamental Mechanisms and Impacts of a Changing Atmosphere. Ph.D. thesis, UC Berkeley.

Seeley, J. T., and N. Jeevanjee, 2021: H2O Windows and CO2 Radiator Fins: A Clear-Sky Explanation for the Peak in Equilibrium Climate Sensitivity. *Geophysical Research Letters*, **48 (4)**, e2020GL089 609, https://doi.org/10.1029/2020GL089609.

Seeley, J. T., N. Jeevanjee, W. Langhans, and D. M. Romps, 2019: Formation of Tropical Anvil Clouds by Slow Evaporation. *Geophysical Research Letters*, **46 (1)**, 492–501, https://doi.org/10.1029/2018GL080747.

Sherwood, S., and Coauthors, 2020: An assessment of Earth's climate sensitivity using multiple lines of evidence. *Reviews of Geophysics*, **n/a (n/a)**, e2019RG000 678, https://doi.org/10.1029/2019RG000678.

Simpson, G., 1928a: Some studies in terrestrial radiation. *Memoirs of the Royal Meteorological Society*, **2 (16)**, 69–95.

Simpson, G. C., 1928b: Further studies in terrestrial radiation. *Memoirs of the Royal Meteorological Society*, **3 (21)**.

Soden, B. J., I. M. Held, R. Colman, K. M. Shell, J. T. Kiehl, and C. A. Shields, 2008: Quantifying Climate Feedbacks Using Radiative Kernels. *Journal of Climate*, **21 (14)**, 3504–3520, https://doi.org/10.1175/2007JCLI2110.1.

Stuecker, M. F., and Coauthors, 2018: Polar amplification dominated by local forcing and feedbacks. *Nature Climate Change*, **8 (12)**, 1076, https://doi.org/10.1038/s41558-018-0339-y.

Tierney, J. E., J. Zhu, J. King, S. B. Malevich, G. J. Hakim, and C. J. Poulsen, 2020: Glacial cooling and climate sensitivity revisited. *Nature*, **584 (7822)**, 569–573, https://doi.org/10.1038/s41586-020-2617-x.

Vallis, G. K., P. Zurita-Gotor, C. Cairns, and J. Kidston, 2014: Response of the large-scale structure of the atmosphere to global warming. *Quarterly Journal of the Royal Meteorological Society*, n/a–n/a, https://doi.org/10.1002/qj.2456.

Wilson, D. J., and J. Gea-Banacloche, 2012: Simple model to estimate the contribution of atmospheric CO2 to the Earth's greenhouse effect. *American Journal of Physics*, **80 (4)**, 306–315, https://doi.org/10.1119/1.3681188.

Zelinka, M. D., T. A. Myers, D. T. McCoy, S. Po-Chedley, P. M. Caldwell, P. Ceppi, S. A. Klein, and K. E. Taylor, 2020: Causes of Higher Climate Sensitivity in CMIP6 Models. *Geophysical Research Letters*, **47 (1)**, e2019GL085 782, https://doi.org/10.1029/2019GL085782.

Zhang, R., H. Wang, Q. Fu, and P. J. Rasch, 2020: Assessing Global and Local Radiative Feedbacks Based on AGCM Simulations for 1980–2014/2017. *Geophysical Research Letters*, **47 (12)**, e2020GL088 063, https://doi.org/10.1029/2020GL088063.